

Field Line Resonance in Two and a Half Dimensions

DRAFT VERSION CREATED ON MARCH 24, 2016

© Charles A. McEachern 2016
ALL RIGHTS RESERVED

Acknowledgements

Acknowledgement placeholder.

Dedication

Dedication placeholder.

Abstract

Abstract placeholder.

Contents

Acknowledgements	i
Dedication	ii
Abstract	iii
List of Tables	vi
List of Figures	vii
1 Introduction	1
1.1 Structure of the Present Work	2
2 The Near-Earth Environment	4
2.1 The Outer Magnetosphere	4
2.2 The Inner Magnetosphere	6
2.3 The Ionosphere	8
2.4 Geomagnetic Storms and Substorms	9
3 Field Line Resonance	11
3.1 Harmonic Structure	14
3.2 Azimuthal Modenumber	16
3.3 Poloidal and Toroidal Polarizations	18
3.4 Giant Pulsations	20
3.5 Motivations for the Present Work	21

4 Waves in a Cold Resistive Plasma	23
4.1 Guided Propagation	25
4.2 Compressional Propagation	26
4.3 High Altitude Limit	28
4.4 Implications to the Present Work	29
5 “Tuna Half” Dimensional Model	31
5.1 Coordinate System	32
5.2 Physical Parameter Profiles	36
5.3 Driving	40
5.4 Maxwell’s Equations	43
5.5 Boundary Conditions	47
6 Electron Inertial Effects	51
6.1 The Boris Factor	52
6.2 Parallel Currents and Electric Fields	54
6.3 Inertial Length Scales	58
7 Numerical Results	61
7.1 Finite Poloidal Lifetimes	61
7.2 Spatial Distribution of Energy	68
7.3 Significance for Giant Pulsations	72
8 Observations	75
8.1 Event Selection	75
8.2 Bias in MLT	77
8.3 Slicing Events One Way...	78
8.4 Slicing Events Another Way...	79
9 Conclusion	82
9.1 Summary of Results	82
9.2 Future Work	82
References	84

List of Tables

3.1	IAGA Magnetic Pulsation Frequency Bands	12
5.1	Typical Parameters for the Tuna Density Profile	37
5.2	Integrated Atmospheric Conductivity	48

List of Figures

2.1	Outer Magnetosphere Cutaway	5
2.2	Inner Magnetosphere Cutaway	7
3.1	Alfvén Bounce Frequencies	13
3.2	First and Second Harmonic Resonances	15
3.3	Large and Small Azimuthal Modenumbers	17
3.4	Poloidal Mode Structure	19
3.5	Toroidal Mode Structure	20
4.1	Compressional Alfvén Wave Cutoff Frequencies	30
5.1	Nonorthogonal Dipole Grid	36
5.2	Alfvén Speed Profiles	38
5.3	Ionospheric Conductivity Profiles	39
5.4	Decreasing Penetration with Increasing Modenumber	41
5.5	Sym-H for June 2013 Storm	42
6.1	Plasma Frequency Profile	53
6.2	Electric Field Snapshots	55
6.3	Current and Poynting Flux at the Ionosphere	56
6.4	Power Density at the Ionosphere	58
6.5	Parallel Electric Fields by Perpendicular Grid Resolution	59
7.1	Poloidal and Toroidal Energy: Quiet Day	63
7.2	Poloidal and Toroidal Energy: Quiet Day, Large Plasmasphere	65
7.3	Poloidal and Toroidal Energy: Quiet Night	67
7.4	Radial Distribution of Poloidal Energy	69
7.5	Radial Distribution of Toroidal Energy	71

7.6	Dayside Ground Magnetic Fields	73
8.1	Spatial Distribution of Usable Van Allen Probe Data	78
8.2	Distribution of Events by Spectral Width	79

Chapter 1

Introduction

TODO: In 1859, humanity was working hard to get its shit together. The United States moved steadily toward the American Civil War, which would abolish slavery and consolidate the power of the federal government. A slew of conflicts in Southern Europe, such as the Austro-Sardinian War, set the stage for the unification of Italy. The Taiping Civil War — one of the bloodiest conflicts of all time — is considered by many to mark the beginning of modern Chinese history. Origin of Species was published. The first transatlantic telegraph cable was laid.

Meanwhile, ambivalent to humanity, the Sun belched an intense burst of charged particles and magnetic energy directly at Earth. The resulting geomagnetic storm¹ caused telegraph systems to fail across the Western hemisphere, electrocuting operators and starting fires[36, 98]. Displays of the northern lights were visible as far south as Cuba.

The Solar Storm of 1859 was perhaps the most powerful in recorded history, but by no means was it a one-time event. The Sun discharges hundreds of coronal mass ejections (CMEs) per year, of all sizes, in all directions. In fact, a comparably large CME narrowly missed Earth in 2012[73]. Had it not, it's estimated it would have caused widespread, long-term electrical outages, with a damage toll on the order of 10^{12} dollars[67].

¹The Solar Storm of 1859 is also called the Carrington Event, after English astronomer Richard Carrington. He drew a connection between the storm's geomagnetic activity and the sunspots he had observed the day before.

The Sun’s extreme — and temperamental — effect on Earth’s magnetic environment makes a compelling case for the ongoing study of space weather. Such research has evolved over the past century from sunspot counts and compass readings to multi-satellite missions and supercomputer simulations. Modern methods have dramatically increased humanity’s understanding of the relationship between the Sun and the Earth; however, significant uncertainty continues to surround geomagnetic storms, substorms, and the various energy transport mechanisms that make them up.

The present work focuses in particular on the phenomenon of field line resonance: Alfvén waves bouncing between the northern and southern hemispheres. Such waves play an important part in the energization of magnetospheric particles, the transport of energy from high to low altitude, and the driving of currents at the top of the atmosphere.

1.1 Structure of the Present Work

TODO: Make this section read nicely.

Chapter 2 briefly introduces the near-Earth environment.

Chapter 3 surveys the field line resonance phenomenon in terms of its underlying physics and notable theoretical and observational work. It also indicates several open questions pertaining to field line resonances.

Chapter 4 explores the fundamental equations of electromagnetic waves in a cold, resistive plasma (such as Earth’s magnetosphere).

Chapter 5 presents a new two and a half dimensional numerical model for the simulation of field line resonances in the inner magnetosphere, particularly those with large azimuthal modenumber.

Chapter 6 shows how electron inertial effects can be added to the model, touches on what can be learned from them, and explains why they are not presently feasible.

Chapter 7 describes the core numerical results of the work, unifying several of the questions posed in Chapter 3.

Chapter 8 puts the numerical results in physical context through the analysis of data from the Van Allen Probes mission.

Chapter 9 briefly summarizes the present work and suggests future directions.

Chapter 2

The Near-Earth Environment

From Earth’s surface to a height of a hundred kilometers or so, the atmosphere is a well-behaved fluid: a collisional ensemble of neutral atoms. Higher up, its behavior changes dramatically. As altitude increases, solar ultraviolet radiation becomes more intense, which ionizes atmospheric atoms. Density also decreases, slowing collisional recombination. Whereas the neutral atmosphere is held against Earth’s surface by gravity, the motion of charged particles is dominated by Earth’s geomagnetic field, as well as the electromagnetic disturbances created as that field is hammered by the solar wind.

The present section outlines the structure of the magnetosphere; that is, the region of space governed primarily by Earth’s magnetic field. Particular emphasis is placed on structures which relate closely to field line resonance.

2.1 The Outer Magnetosphere

Plasma behavior within Earth’s magnetosphere is ultimately driven by the solar wind: a hot (~ 100 eV), fast-moving (~ 100 km/s) plasma threaded by the interplanetary magnetic field (~ 1 nT)¹. The density of the solar wind is on the order of 10^6 /cm³; in a laboratory

¹Listed values correspond to the solar wind at Earth’s orbit.

setting, this would constitute an ultra-high vacuum (atmospheric density at sea level is $\sim 10^{19} \text{ /cm}^3$), but compared to much of the magnetopause it's quite dense.



Figure 2.1: TODO: The outer magnetosphere...

The magnetosphere's outer boundary represents a balance between the solar wind dynamic pressure and the magnetic pressure of Earth's dipole field. On the dayside, the dipole is compressed, pushing this boundary to within about $10 R_E$ of Earth². The nightside magnetosphere is stretched into a long tail which may exceed $50 R_E$ in width and $100 R_E$ in length.

When the interplanetary magnetic field opposes the geomagnetic field at the nose of the magnetosphere, magnetic reconnection occurs. Closed magnetospheric field lines “break,” opening up to the interplanetary magnetic field³. They then move tailward

²Distances in the magnetosphere are typically measured in units of Earth radii: $1 R_E \equiv 6378 \text{ km}$.

³Closed field lines connect at both ends to the magnetic dynamo at Earth's core. Open field lines meet Earth at only one end; the other connects to the interplanetary magnetic field. The distinction is important because charged particle motion is guided by magnetic field lines, as discussed in Chapter 3.

across the poles, dragging their frozen-in plasma with them⁴. Reconnection in the tail allows magnetic field lines to convect back to the day side, across the flanks. This process is called the Dungey cycle[23].

Viewed from the north, the Dungey cycle involves a clockwise flow of flux and plasma on the dusk side and a counterclockwise flow on the dawn side. The motion is accompanied by a convection electric field, per Ohm's law⁵.

TODO: Jets from magnetic reconnection... release of magnetic tension!

Consistent with Ampère's law, the interplanetary magnetic field is separated from the magnetosphere by a current sheet: the magnetopause. On the dayside, the magnetopause current flows duskward; on the nightside, it flows downward around the magnetotail.

Plasma within the tail is cool ($\sim 100 \text{ eV}$) and rarefied ($\sim 10^{-2} / \text{cm}^3$). Earth's dipole is significantly deformed in the magnetotail; field lines in the northern lobe of the tail points more or less Earthward, and vice versa. The two lobes are divided by the plasma sheet, which is comparably hot ($\sim 10^3 \text{ eV}$) and dense ($\sim 1 / \text{cm}^3$). The plasma sheet carries a duskward current which connects to the magnetopause current.

2.2 The Inner Magnetosphere

Within about **TODO: $L \sim 10$** (where L is the McIlwain parameter⁶), the dipole magnetic field is not appreciably deformed by the solar wind. As a result, the structures in the inner magnetosphere follow closely from the motion of charged particles in an ideal dipole field.

⁴In the outer magnetosphere (as well as most of the inner magnetosphere), collisions are so infrequent that magnetic flux is said to be “frozen in” to the plasma. Charged particles move freely along magnetic field lines, but cannot cross from one line to another. Compression of the magnetic field is synonymous with compression of the ambient plasma.

⁵In the case of an ideal plasma, Ohm's law takes the form $\underline{E} + \underline{U} \times \underline{B} = 0$.

⁶The McIlwain parameter L is used to index field lines in Earth's dipole geometry: $L \equiv \frac{r}{\sin^2 \theta}$ for colatitude θ and radius r in Earth radii. For example, the $L = 5$ field line passes through the equatorial plane at a geocentric radius of $5 R_E$, then meets the Earth at a colatitude of $\arcsin \sqrt{\frac{1}{5}} \sim 27^\circ$ (equally, a latitude of $\arccos \sqrt{\frac{1}{5}} \sim 63^\circ$).

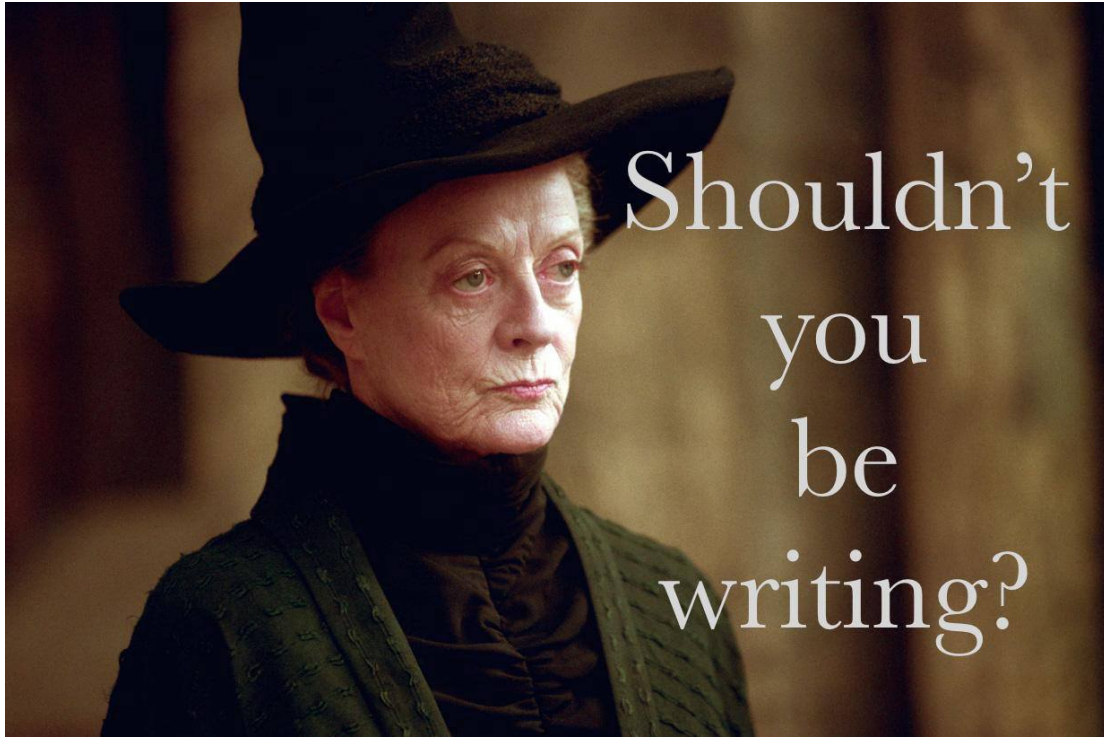


Figure 2.2: TODO: The inner magnetosphere...

The plasmasphere — a cold (~ 1 eV), dense ($10^2 / \text{cm}^3$ to $10^4 / \text{cm}^3$) torus of corotating plasma — is formed by the outward drift of atmospheric ions along magnetic closed field lines. Its outer boundary, is thought to represent a balance between the corotation electric field (per the rotation of Earth's magnetic dipole) and the convection electric field (associated with the convection of magnetic flux during the Dungey cycle). Particle density drops sharply at the edge of the plasmasphere; the boundary is called the plasmapause. The plasmapause typically falls around $L = 4$, though during prolonged quiet times it can extend to $L = 6$ or larger.

Energetic particles trapped within the inner magnetosphere are divided into two populations.

The Van Allen radiation belts are made up of particles with energy above 10^5 eV or so. The inner belt ($L \lesssim 2$) is primarily composed of protons, the decay remnants of

neutrons freed from the atmosphere by cosmic rays. The outer belt ($L \gtrsim 4$) is primarily composed of high-energy electrons.

Particles with energies of 10^3 eV to 10^5 eV make up the ring current, which extends from $L \sim 3$ to $L \sim 5$. Gradient-curvature drift carries ions and electrons in opposite directions; the net result is a westward current. During quiet times, the ring current causes magnetic a southward magnetic field on the order of 1 nT at Earth's equator⁷.

2.3 The Ionosphere

Earth's neutral atmosphere is an excellent insulator. Collisions are so frequent that charged particles quickly thermalize and recombine. The breakdown of air molecules into a conductive plasma (as happens during a lightning strike, for example) requires electric fields on the order of 10^9 mV/m.

Currents are also suppressed by the magnetosphere. In the absence of collisions, electrons and ions drift alongside one another in response to an electric field, creating no net current perpendicular to the magnetic field⁸. Magnetic field lines are (to a good approximation) equipotential contours; electric fields do not form along them to drive parallel currents.

The ionosphere is a sweet spot between the two regimes. Collisions are frequent enough to disrupt the drift of ions, but not frequent enough to immobilize the electrons. The result is nonzero Pedersen and Hall conductivity, corresponding to current along the electric field and in the $\underline{B} \times \underline{E}$ direction respectively. Collisions in the ionosphere also give rise to a finite parallel conductivity, allowing for the formation of potential structures along the magnetic field line.

TODO: Field-aligned currents depend on the level of geomagnetic activity... but do they ever completely go away?

⁷For comparison, Earth's dipole field points north at the equator with a magnitude over 10^4 nT.

⁸The so-called E -cross- B drift is associated with a velocity of $\underline{U} = \frac{1}{B^2} \underline{E} \times \underline{B}$, independent of a charged particle's mass or sign.

The convection electric field (associated with the Dungey cycle, Section 2.1) drives Pedersen currents in the ionosphere. It is these currents that give rise to the strongest magnetic fields on the ground. Pedersen currents flow downward on the flanks and duskward across the poles. The currents remain divergence-free by connecting to field-aligned currents at the edges of the polar cap. The field-aligned currents, in turn, connect to the magnetopause current, the cross-tail current, and the (partial) ring current.

When electron density is low, thermal velocities may be unable to carry enough current to satisfy $\nabla \cdot \underline{J} = 0$. This leads to the formation of potential structures along geomagnetic field lines in the ionosphere. Such structures accelerate particles along magnetic field lines, leading to the precipitation of energetic particles into the atmosphere. As the particles thermalize, they excite atmospheric atoms. The resulting spontaneous emission is often in the visible spectrum, giving rise to the aurora.

TODO: Particles can also be excited by Alfvén waves... this probably goes in Chapter 3.

2.4 Geomagnetic Storms and Substorms

The quiet geomagnetic behavior described above is periodically disturbed by transient solar phenomena such as corotating interaction regions (CIRs) and coronal mass ejections (CMEs). CMEs, as noted in Chapter 1, are bursts of unusually dense solar wind which are ejected from regions of high magnetic activity on the Sun; they are most common at the height of the eleven-year solar cycle. CIRs, on the other hand, occur when a relatively fast region of the solar wind catches up to an earlier and slower-moving pocket of solar wind, resulting in a pair of shockwaves.

During a storm, increased solar wind intensity results in enhanced magnetic reconnection on the dayside. As the newly-opened field lines are swept tailward, the convection electric field is strengthened. The plasmasphere — the outer boundary of which is set by a balance between the convection electric field and the (more or less constant) corotation electric field — sheds its outer layers. A large number of energetic particles are also injected into the ring current[69].

The strength of the storm is gauged by the size of the magnetic perturbation created by the ring current⁹. A small storm has a magnitude of 50 nT to 100 nT. Large storms may reach 250 nT to 500 nT. The Carrington Event, mentioned in Chapter 1, is thought to have exceeded 1700 nT[98].

The main phase of a storm typically lasts for several hours. Storm recovery — the gradual return of the storm index to zero — typically lasts several days. The plasmapause refilling occurs on timescales of **TODO: ???**. Geomagnetic storms occur tens of times per year at the height of the solar cycle, and just a few times per year otherwise.

Whereas storms are prompted by large solar wind events on the dayside, geomagnetic substorms are primarily a nightside occurrence. As flux accumulates in the tail, magnetic tension builds in the stretched field lines. A substorm is an impulsive release of that tension.

TODO: Phases of a substorm. Definition of a substorm comes from [1]. Revised by [70].

At substorm onset, a burst of reconnection occurs in the tail. A jet of plasma is launched Earthward from the reconnection site (and another is launched tailward, and lost to the solar wind). The Earthward plasma injection injects particles into the ring current. The outer radiation belt is depleted, then repopulated. Energetic particles precipitate into the atmosphere, giving rise to a distinctive **TODO: hour-long** sequence of auroral signatures.

Concurrent with substorm onset, impulsive Alfvén waves are observed with periods of a minute or two. The precise ordering of events — whether reconnection causes the waves, or vice versa, or if they share a common cause — remains controversial.

Each substorm lasts several hours, including the time it takes for the ring current to return to pre-substorm levels. Several substorms may occur per day during quiet times. During a storm, substorms become far more frequent; by the time one has ended, another may have already begun.

⁹The most commonly used storm index is Dst, which is computed hourly using measurements from several ground magnetometers near the equator. The Sym-H index, used in Section 5.3, is computed once per minute.

Chapter 3

Field Line Resonance

The motion of a charged particle in a dipole field can be described in terms of three fundamental motions. The first is cyclotron motion: a particle orbits around a magnetic field line in accordance with the Lorentz force. The second is bounce motion: while orbiting, the particle moves along the field line like a bead on a wire, back and forth between the northern and southern hemispheres¹. The third is drift motion: as particles orbit and bounce, they also move azimuthally around Earth per the gradient-curvature drift.

Characteristic timescales for each of the above motions depend on particle energy. Electron cyclotron motion is on the order of `TODO: ...` in the ionosphere, and closer to `TODO: ...` in the tail; ions gyrate slower by three orders of magnitude due to their larger mass. `TODO: Bounce... Drift...`

Wave-particle resonance arises when a particle's periodic motion matches with the frequency of a coincident electromagnetic wave[25, 64, 75, 87]. In the particle's rest frame, the wave then appears as a net electric field. This allows a net movement of energy

¹As a particle approaches Earth, it experiences an ever-stronger magnetic field. The particle's perpendicular kinetic energy increases in proportion with the magnetic field in order to conserve its first adiabatic invariant. When the perpendicular kinetic energy can no longer increase — that is, when the parallel kinetic energy is zero — the particle bounces back. (If the parallel kinetic energy is sufficiently large, the particle doesn't bounce; it precipitates into the atmosphere.)

between the wave and the particle. The interaction is analogous to a surfer moving along with — and being accelerated by — a wave in the ocean.

In the present work, the waves in question are field line resonances (FLRs). An FLR is a standing harmonic on a geomagnetic field line. It can also be envisioned as a superposition of traveling waves, reflecting back and forth between its northern and southern foot points at the conducting ionosphere. These waves travel at the Alfvén speed². The fundamental equations of field line resonance were presented by Dungey in 1954[22]; since then, they have remained a topic of active study.

So-called ultra low frequency waves — of which FLRs are a subset — are categorized by morphology. Continuous (long-lived) pulsations are termed Pc, while irregular pulsations are called Pi. Within each are a number of frequency bands; see Table 3.1[45].

Table 3.1: IAGA Magnetic Pulsation Frequency Bands

	Pc1	Pc2	Pc3	Pc4	Pc5	Pi1	Pi2
Period (s)	0.2–5	5–10	10–45	45–150	150–600	1–40	40–150
Frequency (mHz)	200–5000	100–200	22–100	7–22	2–7	25–1000	7–25

FLRs fall into the Pc3, Pc4, and Pc5 ranges. The present work focuses specifically on the Pc4 band: waves with periods of a minute or two. Frequencies in the Pc4 range typically coincide with Alfvén bounce times³ near the plasmapause: $L \sim 4$ to $L \sim 6$ [3, 17, 26, 56]⁴. In fact, the large radial gradients in the Alfvén speed near the plasmapause act as an effective potential well, trapping FLRs[16, 50, 53, 54, 63, 90].

In addition to being radially localized, FLRs in the Pc4 frequency band (also called Pc4 pulsations, or just Pc4s) are localized in magnetic local time (MLT⁵). They have also

²The Alfvén speed is given by v_A is given by $v_A^2 \equiv \frac{B^2}{\mu_0 \rho}$, where B is the magnitude of the magnetic field, μ_0 is the magnetic constant, and ρ is the mass density of the ambient plasma. It can vary by several orders of magnitude over the length of a magnetic field line.

³The Alfvén frequency is the inverse of the Alfvén bounce time: $\frac{2\pi}{\omega_A} \equiv \oint \frac{dz}{v_A}$.

⁴Not coincidentally, these are the same L -shells where the Van Allen Probes spend most of their time; see Chapter 8.

⁵Noon points toward the Sun and midnight away from it, with 06:00 and 18:00 at the respective dawn and dusk flanks.

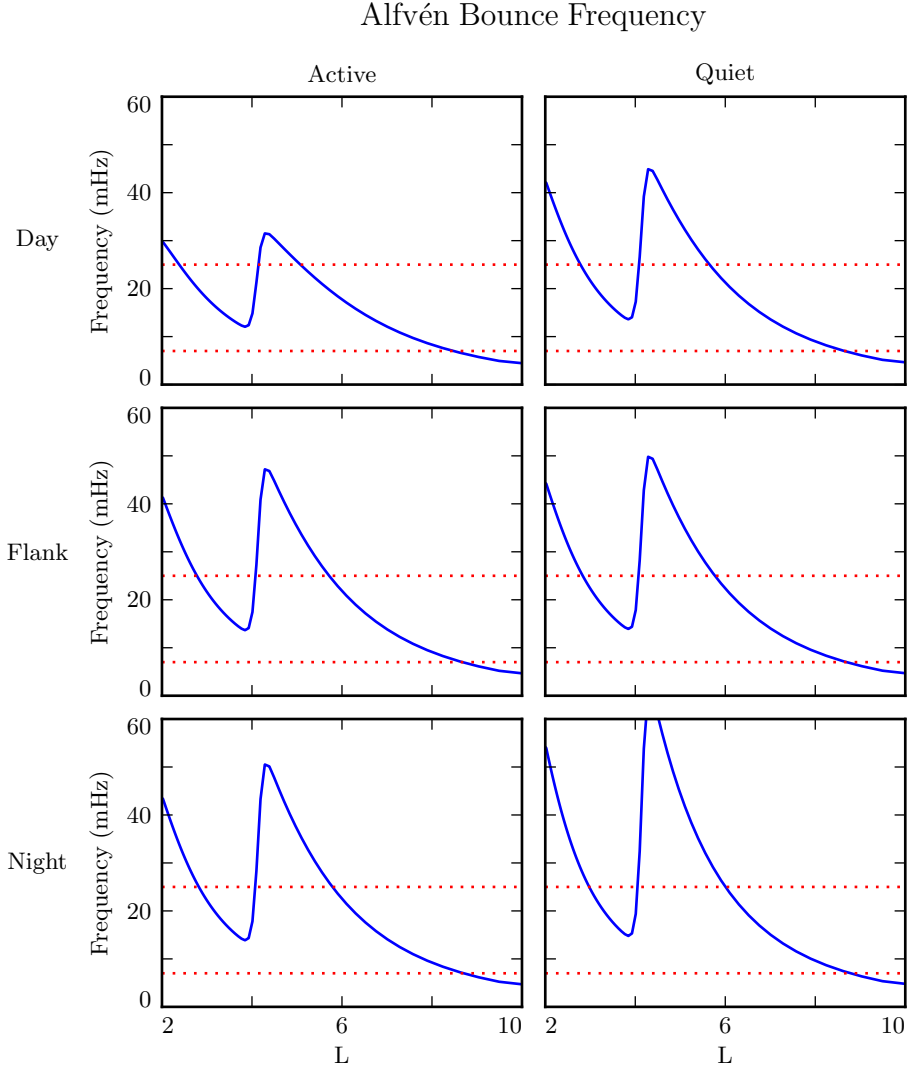


Figure 3.1: The above are bounce frequencies for an Alfvén wave moving back and forth along a geomagnetic field line. Alfvén speeds are computed based on profiles from Kelley[48], as discussed in Section 5.2. Notably, the bounce frequency depends significantly on the position of the plasmasphere, taken here to be at $L = 4$. Dotted lines indicate the Pc4 frequency range: 7 mHz to 25 mHz.

been shown to occur preferentially on the dayside, during storms or storm recovery[3, 17, 26, 52, 56, 99].

In the inner magnetosphere, the Alfvén frequency — and thus the frequency of FLRs — often coincides with integer or half-integer⁶ multiples of particle drift frequencies[18]. The resulting wave-particle interactions can give rise to significant energization and radial diffusion of the particles. In some cases, the waves also include an electric field parallel to the background magnetic field, contributing to the precipitation of energetic particles into the neutral atmosphere[33, 34, 95, 104].

The present chapter introduces the structural characteristics of FLRs, how those characteristics affect wave behavior, and several unresolved questions related to that behavior.

TODO: Other planets[32]? Seems exciting but maybe not relevant.

3.1 Harmonic Structure

Wave structure along a geomagnetic field line is indicated by harmonic number. The first (or fundamental) harmonic has a wavelength twice as long as the field line. It exhibits an antinode in the perpendicular electric field at the equator, along with a node in the perpendicular magnetic field. The second harmonic is a single wavelength along the field line. Its perpendicular magnetic perturbation has an antinode at the equator, while its perpendicular electric field has a node. Figure 3.2 shows a qualitative sketch of each: a series of snapshots in time, in the rest frame of the wave. Perpendicular electric and magnetic field perturbations are shown in blue and red respectively.

A first-harmonic FLR that is periodic or localized in the azimuthal direction is conducive to drift-resonant wave-particle interactions[18, 77]. The particle is like a child on a swing: whenever the path of the particle (or child) gets close to the wave (parent), it gets a push, and always in the same direction. The wave fields spend half its time pointing the other direction, just as the parent must shift their weight backward to get ready for the next push, but at that point the particle (child) is far away.

Second-harmonic FLRs interact with particles through the drift-bounce resonance, which is slightly more complicated. As the particle drifts azimuthally, it also zig-zags north-south. The combination of those two periodic motions must align with the phase of

⁶See Section 3.1.

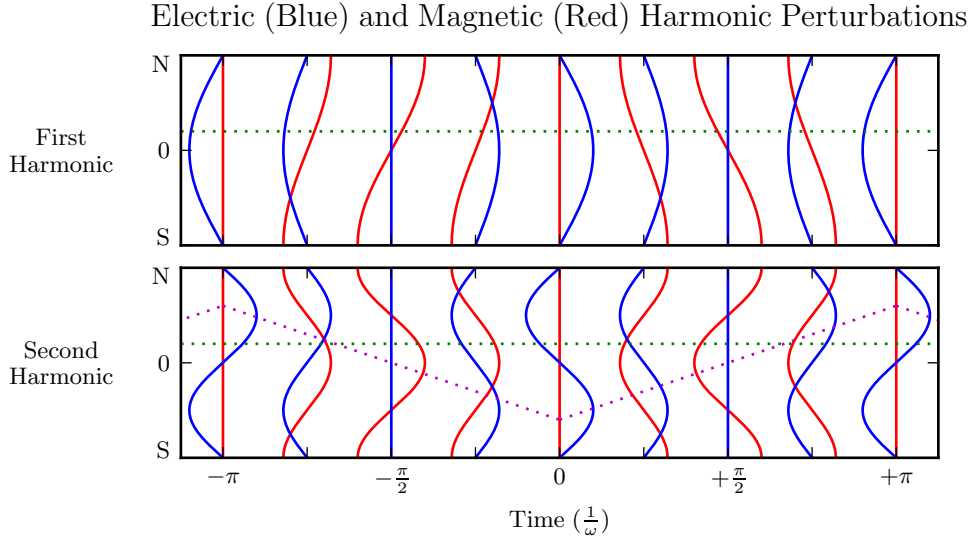


Figure 3.2: The first (or fundamental) harmonic has an antinode in its perpendicular electric field (blue) at the equator, along with a node in its perpendicular magnetic field perturbation (red). A single satellite can identify the first harmonic by the relative phase of the electric and magnetic field perturbations: an observer north of the equator (green) will see the electric field perturbation lead the magnetic field by 90° . The second harmonic is the opposite: it has an electric field node at the equator, and an observer north of the equator will see the electric field perturbation lag the magnetic field by 90° . The purple line sketches the path of a particle in drift-bounce resonance; in the particle’s rest frame, the electric field is always to the right.

the wave electric field. An example path is shown by the purple line in Figure 3.2: the particle experiences a rightward electric field throughout the wave’s oscillation.

The drift-bounce resonance condition is written[91]:

$$\omega - m\omega_D = \omega_B \quad (3.1)$$

Where ω is the frequency of the wave, ω_D and ω_B are the particle’s drift and bounce frequencies respectively, and m is the wave’s azimuthal modenumber, as discussed in Section 3.2.

In principle, the first and second harmonics can be distinguished by their frequencies, even from a single-point observation[15, 35]. In practice, however, this is not a reliable approach[92]. There are significant uncertainties surrounding the number density profile — and thus the Alfvén speed profile — along a geomagnetic field line.

Harmonic structure can also be deduced by noting the phase offset between the wave magnetic field and its electric field (or the plasma velocity)[17, 94]. In Figure 3.2, the green line indicates an observer just north of the magnetic equator. For the first harmonic, the observer sees the electric field waveform lead the magnetic field by a phase of 90° ; for the second harmonic, the electric field waveform lags by 90° . (South of the equator, the signs are reversed.) Notably, this approach has only become viable with the advent of satellites carrying both electric and magnetic field instrumentation, such as THEMIS in 2007[4] and the Van Allen Probes⁷ in 2012[88].

Strictly speaking, the the phase offset of the electric and magnetic fields does not provide the harmonic number — only its parity. It's reasonably safe to assume that an even mode is the second harmonic; the second harmonic is by far the most commonly observed[44, 85, 93], due in part to its excitement by the antisymmetric balloon instability[9, 11, 13, 87]. However, the distinction between the first and third harmonics is not always clear; this issue is discussed further in Chapter 8. Higher harmonics than that are not expected in the Pc4 frequency band.

TODO: Second-harmonic FLRs are unlikely to cause ground signatures[94].

TODO: Dai found a nice event[18] that was unambiguously determined to be a fundamental-mode Pc4 in drift-resonant interaction with $\sim 10^5$ eV ions. Consistent with [96]. Other observations of odd harmonics: [105, 27].

3.2 Azimuthal Modenumber

The wavelength of an FLR in the azimuthal direction is indicated by its azimuthal wavelength. A wave with modenumber m has an azimuthal wavelength that spans $\frac{24}{m}$ hours in MLT.

⁷The Van Allen Probes were previously called RBSP, for Radiation Belt Storm Probes.

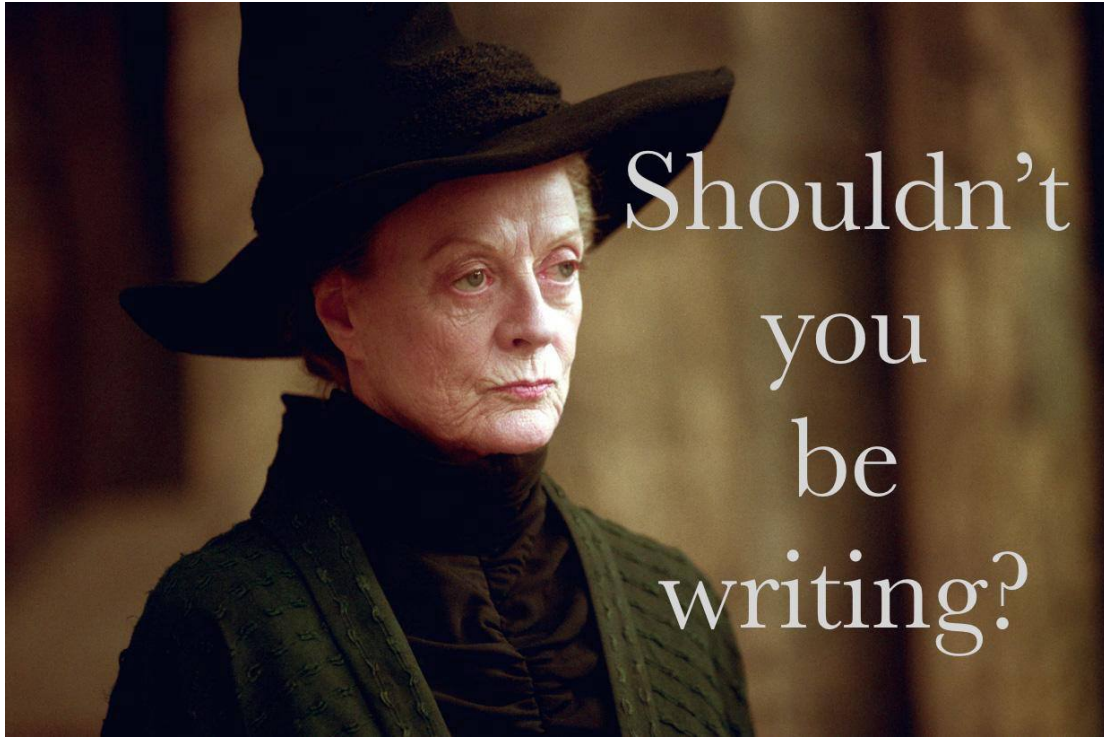


Figure 3.3: TODO: ...

Waves with small azimuthal modenumbers ($0 < m < 10$) are typically driven by broadband energy sources at the magnetosphere's boundary, such as variations in the solar wind pressure[19, 39, 49, 108, 109], sporadic magnetic reconnection[42], or Kelvin-Helmholtz waves on the magnetopause[10, 58, 86]. In the low- m regime, the shear and compressional Alfvén waves are coupled, which allows energy to move across field lines until the driving frequency lines up with the local Alfvén frequency[60]. Because of their broadband energy source, low- m FLRs often have a mishmash of frequencies present in their spectra[17].

When the azimuthal modenumber is large (or, equally, when the azimuthal wavelength is small), the shear and compressional Alfvén waves are decoupled[15, 80]⁸. As a result, FLRs must be driven from within the magnetosphere. Proposed energy sources include

⁸Equally, the strength of a wave's parallel component hint at its modenumber, a point which is revisited in Chapter 8.

phase space gradients near the plasmapause[18], particularly as the plasmasphere refills after a storm or substorm[26, 55].

The ionosphere is known to attenuate waves with small spatial extent in the perpendicular direction[43, 103, 107]. As a result, FLRs may create no signature on the ground if their azimuthal modenumber is large. For example, a recent paper by Takahashi shows a strong (2 nT at $L \sim 10$), clear resonance with $|m| \gtrsim 70$ and no corresponding ground signature[92].

Southwood[87] and Glassmeier[30] show that a low frequency wave passing through the ionosphere on its way to Earth will be attenuated per

$$\frac{B_E}{B_I} = \frac{\Sigma_H}{\Sigma_P} \exp\left(-m \frac{R_I - R_E}{R_E \sin \theta}\right) \quad (3.2)$$

Where B_E and B_I are the magnetic field strengths at R_E (Earth's surface, 6783 km geocentric) and R_I (the ionosphere, \sim 6900 km geocentric) respectively. The integrated ionospheric Pedersen and Hall conductivities, Σ_P and Σ_H , are typically within a factor of two of one another. Field lines near the plasmapause can be traced to Earth at $\sin \theta \sim 0.4$. That is, by the time it reaches the ground, the magnetic field from an FLR with $m = 10$ is weaker by a factor of two; at $m = 100$, the factor is closer to 100.

3.3 Poloidal and Toroidal Polarizations

Based on polarization, each FLR can be classified as either poloidal or toroidal. The poloidal mode is a field line displacement in the meridional plane, as shown in Figure 3.4, with an accompanying electric field in the azimuthal direction. The toroidal mode's magnetic displacement is azimuthal, per Figure 3.5; the associated electric field is in the meridional plane.

Both poloidal and toroidal waves are noted for their ability to contribute to the energization and radial diffusion of trapped particles. The poloidal mode interacts more strongly,

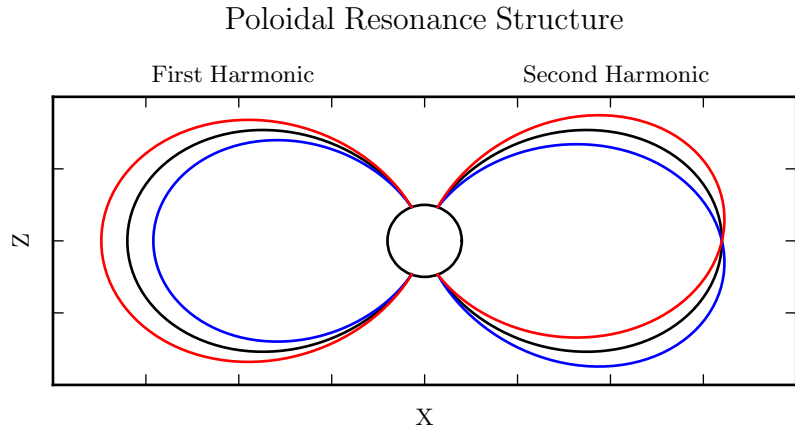


Figure 3.4: The poloidal resonance is a magnetic field in the meridional plane. The displacement is radial near the equator, and can be accompanied by enhancement in the parallel magnetic field near the ionosphere. The first harmonic is shown on the left, and the second harmonic on the right. Lines are colored red and blue only to contrast with the unperturbed black field line.

since its electric field is aligned with the trapped particles’ drift motion. Poloidally-polarized waves are also more prone to creating magnetic signatures on the ground, due to ducting in the ionosphere[28, 37].

Toroidal modes have been shown to far outnumber poloidal modes[3]. Perhaps not coincidentally, poloidally-polarized waves rotate asymptotically to the toroidal mode[65, 66, 80]. Poloidal waves with low azimuthal modenumber — such as those driven by broadband sources at the magnetopause — rotate on timescales comparable to their oscillation periods.

TODO: Fishbone instability[12, 68]. Like the poloidal mode, but for lab plasmas.

TODO: Poloidal and toroidal modes are coupled by the ionospheric Hall conductivity[47]. The Hall conductivity also increases the “ringtime” of these resonances, allowing them to oscillate through the inductive process rather than be dissipated as Joule heating[101].

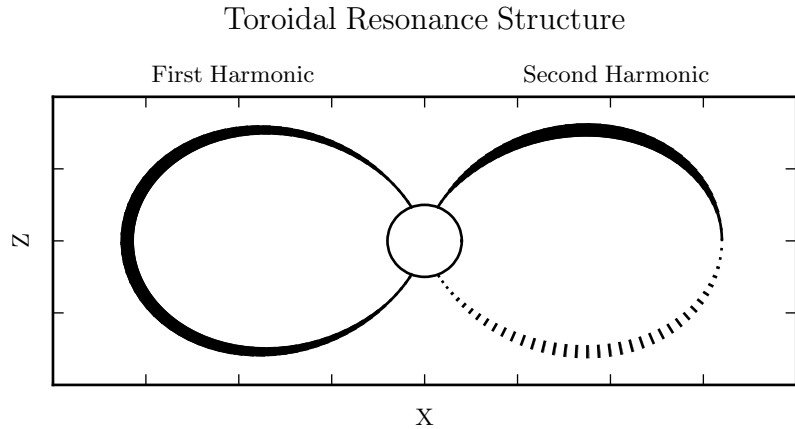


Figure 3.5: A toroidally-polarized FLR has a magnetic perturbation in the azimuthal direction, as shown. Bold lines are taken to be above the page, and dotted lines below the page, with the displacement indicated by the line’s width. The first harmonic — where the entire field line oscillates in and out of the page — is shown on the left. The second harmonic is on the right, with northern and southern halves perturbed in opposite directions.

3.4 Giant Pulsations

The study of geomagnetic pulsations long predates satellites, sounding rockets, or even the word “magnetohydrodynamics”⁹. Large, regular oscillations in the magnetic field were noted as early as 1901[5]. Eventually, the term “giant pulsation,” or Pg, arose to describe such pulsations.

On the ground, Pgs are notable for their strikingly sinusoidal waveforms, their eastward drifts, and their specific occurrence pattern: Pgs are typically seen pre-dawn, at latitudes of 60° to 70° . Pgs generally fall into the Pc4 frequency band¹⁰. Their harmonic structure was a source of controversy for decades, but recent multisatellite observations seem to be in agreement that they are odd harmonics, probably fundamental[31, 41, 51, 52, 91, 94]. They are poloidally polarized, with modenumbers $10 \lesssim m \lesssim 40$ [29, 41, 77, 83, 94].

⁹The term was first used by Alfvén in the 1940s[2].

¹⁰The Pc4 range is periods of 45 s to 140 s, while Pgs are often said to range from 60 s to 200 s[7].

Whereas FLRs are waves in space which may produce ground signatures, “giant pulsation” refers to the ground signature specifically¹¹. That is, Takahashi’s satellite observation of a sinusoidal, morningside, high- m , fundamental poloidal resonance was not classified as a Pg because it did not produce a signal on the ground[92].

Due to their remarkably clear waveforms, Pgs are typically found by “visual inspection of magnetometer data”[71]. Over the course of the past century, a number of multi-year (sometimes multi-decade[7]) surveys have totaled nearly one thousand Pg events. On average, a ground magnetometer near 66° magnetic latitude observes ~ 10 Pg events per year[7, 40, 82, 89]. Observations are not distributed uniformly; rather, giant pulsations become more common near the equinox and during times of low solar activity.

Unlike Pc4 pulsations in general, Pgs show no particular correlation with storm phase[71]. However, they do often occur as the magnetosphere recovers from a substom[71, 83].

3.5 Motivations for the Present Work

A great deal has been learned — and continues to be learned — through observations of field line resonance. However, the cost-to-benefit ratio is climbing. As summarized in the sections above, FLR behavior depends significantly on harmonic structure, azimuthal modenumber, and polarization — not to mention frequency, spectral width, and so on. With each degree of freedom comes the necessity for an additional simultaneous observation.

Similarly, as FLRs have been shown to depend on ever-more-specific magnetospheric conditions, analytical techniques have fallen out of favor. The height-resolved ionosphere, the multidimensional Alfvén speed profile, and the inconvenient geometry combine to create a problem beyond the reasonable purview of pencil and paper.

That is, the topic of field line resonance is ripe for numerical modeling.

¹¹Historically, the wave designations shown in Table 3.1 all referred to ground phenomena. Over time, they have come to describe satellite observations as well, including those without corresponding signatures on the ground.

Past models of the magnetosphere have been ill-suited for the consideration of FLRs. Reasons include overly-simplified treatment of the ionospheric boundary, no consideration of the plasmapause, limited range in m , and the inability to compute ground signatures. Chapter 5 presents a model which addresses these issues, allowing the computation of field line resonance with unparalleled attention to realism.

The model allows a bird's-eye view of the structure and evolution of FLRs. As such, not only can several open questions be addressed, but their answers serve to unify a number of seemingly-disparate properties described in the sections above.

The rotation of poloidally-polarized waves to the toroidal mode is investigated. Particular attention is paid to the importance of azimuthal modenumber and ionospheric conductivity. The interplay between said rotation and the transport of energy across field lines — which also depends on azimuthal modenumber — is considered as well.

By their nature, drifting particles have the potential to spur wave-particle interactions at all MLT. However, Pc4 observations are strongly peaked on the dayside. In a 2015 paper, Dai notes, “It is not clear why noncompressional [high- m] Pc4 poloidal waves, which are presumably driven by instability within the magnetosphere, preferentially occur on the dayside”[17]. Motoba, later that year, echoes, “It is unclear whether other generation mechanisms of fundamental standing waves ... can explain the localization of Pgs in local time”[71]. This, too, is considered numerically: to what degree is field line resonance affected by the (day-night asymmetric) conditions of the ionosphere?

TODO: Transition... With the above in mind, what data would be super helpful?

It’s been shown that a ground magnetometer 66° north of the magnetic equator observes \sim 10 Pg events per year. It’s also been shown that poloidal Pc4s are rare compared to toroidal ones, and that most poloidal Pc4s are even harmonics. However, little attention has been paid to how these rates line up with one another. Given the relative occurrence rate of poloidal and toroidal waves, of odd and even harmonics, and of diffuse and sharp spectral peaks, just how unusual are giant pulsations?

Chapter 4

Waves in a Cold Resistive Plasma

Before delving into the implementation of the numerical model, it's instructive to consider the fundamental equations of waves in a cold, resistive plasma.

The evolution of electric and magnetic fields is governed by Ampère's law and Faraday's law. Notably, the present work takes the linearized versions of Maxwell's equations; the vectors \underline{E} and \underline{B} indicate perturbations above the zeroth-order magnetic field.

$$\underline{\epsilon} \cdot \frac{\partial}{\partial t} \underline{E} = \frac{1}{\mu_0} \nabla \times \underline{B} - \underline{J} \quad \frac{\partial}{\partial t} \underline{B} = -\nabla \times \underline{E} \quad (4.1)$$

Current follows Ohm's law. For currents perpendicular to the background magnetic field, Kirchhoff's formulation is sufficient. Conductivity is much higher along the magnetic field lines¹, so it's appropriate to also include the electron inertial term².

$$0 = \underline{\sigma}_{\perp} \cdot \underline{E}_{\perp} - \underline{J}_{\perp} \quad \frac{1}{\nu} \frac{\partial}{\partial t} J_z = \sigma_0 E_z - J_z \quad (4.2)$$

¹The dipole coordinate system is defined rigorously in Section 5.1; at present, it's sufficient to take \hat{z} parallel to the zeroth-order magnetic field, and \hat{x} and \hat{y} perpendicular to \hat{z} (and to each other).

²Electron inertial effects are not included in the model described in Chapter 5, or in the results in Chapter 7; however, their implementation and impact are explored in Chapter 6.

Derivatives in Equations (4.1) and (4.2) can be evaluated by performing a Fourier transform. They can then be combined, eliminating the magnetic field and current terms.

$$\begin{aligned} 0 &= \underline{\underline{E}}_{\perp} + \frac{v_A^2}{\omega^2} (\underline{k} \times \underline{k} \times \underline{E})_{\perp} + \frac{i}{\epsilon_{\perp}\omega} \underline{\sigma}_{\perp} \cdot \underline{E}_{\perp} \\ 0 &= E_z + \frac{c^2}{\omega^2} (\underline{k} \times \underline{k} \times \underline{E})_z + \frac{i\omega_P^2}{\omega(\nu - i\omega)} E_z \end{aligned} \quad (4.3)$$

The speed of light, Alfvén speed (including the displacement current correction), plasma frequency, and parallel conductivity are defined in the usual way:

$$c^2 \equiv \frac{1}{\mu_0\epsilon_0} \quad v_A^2 \equiv \frac{1}{\mu_0\epsilon_{\perp}} \quad \omega_P^2 \equiv \frac{ne^2}{m_e\epsilon_0} \quad \sigma_0 \equiv \frac{ne^2}{m_e\nu} \quad (4.4)$$

Using the vector identity $\underline{k} \times \underline{k} \times \underline{E} = \underline{k} \underline{k} \cdot \underline{E} - k^2 \underline{E}$, Equation (4.3) can be reassembled into a single expression,

$$0 = \left(\underline{\underline{\mathbb{I}}} + \frac{1}{\omega^2} \underline{\underline{V}}^2 \cdot \underline{k} \underline{k} - \frac{k^2}{\omega^2} \underline{\underline{V}}^2 + \frac{i}{\omega} \underline{\underline{\Omega}} \right) \cdot \underline{E} \quad (4.5)$$

Where $\underline{\underline{\mathbb{I}}}$ is the identity tensor and in x - y - z coordinates,

$$\underline{\underline{V}}^2 \equiv \begin{bmatrix} v_A^2 & 0 & 0 \\ 0 & v_A^2 & 0 \\ 0 & 0 & c^2 \end{bmatrix} \quad \text{and} \quad \underline{\underline{\Omega}} \equiv \begin{bmatrix} \frac{\sigma_P}{\epsilon_{\perp}} & \frac{-\sigma_H}{\epsilon_{\perp}} & 0 \\ \frac{\sigma_H}{\epsilon_{\perp}} & \frac{\sigma_P}{\epsilon_{\perp}} & 0 \\ 0 & 0 & \frac{\omega_P^2}{(\nu - i\omega)} \end{bmatrix} \quad (4.6)$$

In Equation (4.5), the expression in parentheses is the dispersion tensor. Nontrivial solutions exist only when its determinant is zero. This gives rise to a seventh-order polynomial in ω , so rather than a direct solution it's necessary to consider limits of specific interest.

Without loss of generality, the wave vector \underline{k} may be taken to lie in the x - z plane — that is, with $k_y = 0$. The distinction between the two perpendicular directions is discussed in Section 4.4.

4.1 Guided Propagation

The wave vector of a field line resonance aligns closely to the background magnetic field. By supposing that the two align exactly (that is, taking $k_x = 0$), the parallel and perpendicular components of the dispersion relation are decoupled.

The parallel-polarized component — that is, the solution when $E_x = E_y = 0$ — is quadratic, and thus can be solved directly.

$$0 = \omega^2 + i\nu\omega - \omega_P^2 \quad \text{so} \quad \omega = -\frac{i\nu}{2} \pm \sqrt{\omega_P^2 - \frac{\nu^2}{4}} \quad (4.7)$$

It bears noting that the plasma frequency is large — not just compared to Pc4 frequencies, but even compared to the collision frequencies in the ionosphere³.

Expanding Equation (4.7) with respect to large ω_P , the dispersion relation becomes

$$\omega^2 = \omega_P^2 \pm i\nu\omega_P + \dots \quad (4.8)$$

Equation (4.8) can hardly be called a wave, as it does not depend on the wave vector \underline{k} . Rather, it is the plasma oscillation⁴: electrons vibrating in response to a charge separation along the background magnetic field.

The plasma oscillation is not specifically relevant to the study of field line resonance. The two phenomena are separated by six orders of magnitude in frequency. The topic is revisited in Chapter 6 insomuch as it is inseparable from the electron inertial effects in Ohm's law.

³The collision frequency may match or exceed the plasma frequency for a thin slice at the bottom of the ionosphere, where the density of neutral atoms is large; however, it falls off quickly. Above an altitude of 200 km, conservatively[74], the plasma frequency exceeds the collision frequency by an order of magnitude or more.

⁴The plasma oscillation is also called the Langmuir wave, after Irving Langmuir.

The perpendicular ($E_z = 0$) components of the dispersion relation give an expression quartic in ω .

$$0 = \omega^4 + 2i\frac{\sigma_P}{\epsilon_\perp}\omega^3 - \left(2k_z^2v_A^2 + \frac{\sigma_P^2 + \sigma_H^2}{\epsilon_\perp^2}\right)\omega^2 - 2ik_z^2v_A^2\frac{\sigma_P}{\epsilon_\perp}\omega + k_z^4v_A^4 \quad (4.9)$$

Like the parallel-polarized component above, Equation (4.9) can be solved directly. Noting that \pm and \oplus are independent,

$$\omega = \left(\frac{\pm\sigma_H - i\sigma_P}{2\epsilon_\perp}\right) \oplus \sqrt{k_z^2v_A^2 + \left(\frac{\pm\sigma_H - i\sigma_P}{2\epsilon_\perp}\right)^2} \quad (4.10)$$

Also like the parallel-polarized component, the exact solution is less useful than its Taylor expansion. The Pedersen and Hall conductivities are large near the ionospheric boundary, but fall off quickly; for the vast majority of the field line, the ratios $\frac{\sigma_P}{\epsilon_\perp}$ and $\frac{\sigma_H}{\epsilon_\perp}$ are small compared to field line resonance frequencies. Expanding with respect to small conductivity gives

$$\omega^2 = k_z^2v_A^2 \oplus k_zv_A\frac{\sigma_H \pm i\sigma_P}{\epsilon_\perp} + \dots \quad (4.11)$$

This is the shear Alfvén wave, with a shift to its frequency due to the conductivity of the ionosphere. It travels along the background magnetic field like a bead on a string, with electric and magnetic field perturbations perpendicular to the magnetic field line (and to one another).

4.2 Compressional Propagation

The partner to guided motion is compressional motion; in order for energy to move across field lines, the wave vector must have a component perpendicular to \hat{z} . If the wave vector is completely perpendicular to the magnetic field line ($k_z = 0$), the parallel and perpendicular components of the dispersion relation decouple, as in Section 4.1.

The parallel-polarized ($E_x = E_y = 0$) component of the dispersion relation is

$$0 = \omega^3 + i\nu\omega^2 - (k_x^2 c^2 + \omega_P^2) \omega - ik_x^2 c^2 \nu \quad (4.12)$$

Equation (4.12) can be solved directly, though its solution (as a cubic) is far too long to be useful. Expanding with respect to the large plasma frequency, gives

$$\omega^2 = k^2 c^2 + \omega_P^2 - i\nu\omega_P + \dots \quad (4.13)$$

This is the O mode, a compressional wave with an electric field perturbation along the background magnetic field. Like the plasma oscillation discussed in Section 4.1, its frequency is very large compared to that of a field line resonance.

The perpendicular-polarized ($E_z = 0$) component of the compressional dispersion relation is also cubic.

$$0 = \omega^3 + 2i\frac{\sigma_P}{\epsilon_\perp}\omega^2 - \left(2k_x^2 v_A^2 + \frac{\sigma_P^2 + \sigma_H^2}{\epsilon_\perp^2}\right)\omega - ik_x^2 v_A^2 \frac{\sigma_P}{\epsilon_\perp} \quad (4.14)$$

A wave moving across magnetic field lines near the ionospheric boundary will encounter large $\frac{\sigma_P}{\epsilon_\perp}$ and $\frac{\sigma_H}{\epsilon_\perp}$, while at moderate to high altitudes those ratios will be small. Solving Equation (4.14) in those two limits respectively gives:

$$\omega^2 = k_x^2 v_A^2 \pm ik_x v_A \frac{\sigma_P}{\epsilon_\perp} + \dots \quad \text{and} \quad \omega^2 = k_x^2 v_A^2 + \left(\frac{\sigma_H \pm i\sigma_P}{\epsilon_\perp}\right)^2 + \dots \quad (4.15)$$

In both limits, Equation (4.15) describes a compressional Alfvén wave. The magnetic field perturbation is along the background magnetic field — indicating compression of the frozen-in plasma — while the electric field perturbation is perpendicular to both the magnetic field and the wave vector.

TODO: Double check terminology. Jesse's dissertation disagrees with Bob's notes.

4.3 High Altitude Limit

In the limit of large radial distance, it's reasonable to take the collision frequency to zero; doing so also neglects the Pedersen and Hall conductivities.

Whereas in Sections 4.1 and 4.2 it was the parallel-polarized component of the dispersion relation that factored out from the other two, the high altitude limit decouples the component polarized out of the x - z plane. The y -polarized dispersion ($E_x = E_z = 0$) is simply:

$$\omega^2 = k^2 v_A^2 \quad (4.16)$$

Equation (4.16) describes an Alfvén wave with an arbitrary angle of propagation. Depending on the angle between the wave vector and the background magnetic field, it could be guided, compressional, or somewhere in between. Regardless of propagation angle, the electric field perturbation is perpendicular to both the direction of propagation and the magnetic field perturbation.

The other two components (from $E_y = 0$) of the high altitude dispersion tensor give an expression quadratic in ω^2 :

$$0 = \omega^4 - (k_x^2 c^2 + k_z^2 v_A^2 + \omega_P^2) \omega^2 + k_z^2 v_A^2 \omega_P^2 \quad (4.17)$$

Which can be solved for

$$\omega^2 = \frac{1}{2} (k_x^2 c^2 + k_z^2 v_A^2 + \omega_P^2) \pm \sqrt{\frac{1}{4} (k_x^2 c^2 + k_z^2 v_A^2 + \omega_P^2)^2 - k_z^2 v_A^2 \omega_P^2} \quad (4.18)$$

Noting again that ω_P is very large, the two roots can be expanded to

$$\omega^2 = k_z^2 v_A^2 \left(1 + \frac{k_x^2 c^2 + k_z^2 v_A^2}{\omega_P^2} \right) + \dots \quad \text{and} \quad \omega^2 = k_x^2 c^2 + k_z^2 v_A^2 + \omega_P^2 + \dots \quad (4.19)$$

The first is a shear Alfvén wave, as in Equation (4.11). The second oscillates faster than the plasma frequency; like the plasma oscillation in Equation (4.8) and the O mode in Equation (4.13), it's far outside the Pc4 frequency range.

4.4 Implications to the Present Work

The present section's findings carry three significant implications for the present work.

First — with the exception of the plasma oscillation and similar modes, which are revisited in Chapter 6 — waves propagate at the Alfvén speed. This, in combination with the grid configuration, will constrain the time step that can be used to model them numerically. The time step must be sufficiently small that information traveling at the Alfvén speed cannot “skip over” entire grid cells⁵.

Second, the results of the present section allow an estimate of the magnitude of parallel electric field that might be expected from a field line resonance compared to its perpendicular electric field. Between the full dispersion tensor form in Equation (4.5) and the Alfvén wave described by Equation (4.19),

$$\left| \frac{E_z}{E_x} \right| = \frac{k_x k_z c^2}{\omega^2 - k_x^2 c^2 - \omega_P^2} \sim \frac{k^2 c^2}{\omega_P^2} \quad (4.20)$$

In essence, the relative magnitudes of the parallel and perpendicular electric fields should be in proportion to the square of the relative magnitudes of the electron inertial length (1 km to 100 km) and the wavelength ($\sim 10^5$ km). That is, parallel electric fields should be smaller than the perpendicular electric fields by six or more orders of magnitude.

Finally, the dispersion relations shown above indicate how the behavior of a field line resonance should behave as the azimuthal modenumber becomes large.

Whereas the shear Alfvén wave's dispersion relation depends only on the parallel component of the wave vector, the compressional Alfvén wave depends on its magnitude: $\omega^2 = k^2 v_A^2$. If the frequency is smaller than $k v_A$, the wave will become evanescent. The

⁵As is the convention, the time step is scaled down from the smallest Alfvén zone crossing time by a Courant factor, typically 0.1, meaning that it takes at least ten time steps to cross a grid cell.

wave vector's magnitude can be no smaller than its smallest component, however, and the azimuthal component scales with the azimuthal modenumber: $k_y \sim \frac{m}{2\pi r}$.

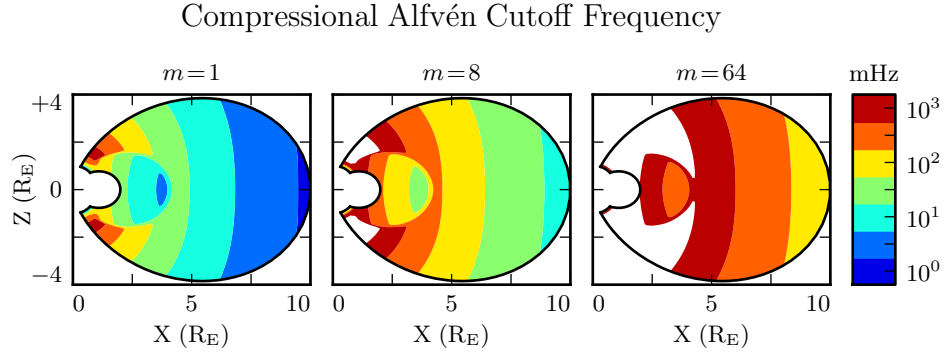


Figure 4.1: Taking $k_y \sim \frac{m}{2\pi r}$ as a lower bound for the magnitude of the wave vector, the above figure demonstrates the lowest frequency at which compressional Alfvén waves may propagate as a function of position and m . Regions shown in white are off the color scale — they have a lower bound on the order of 10^4 mHz or more. Alfvén frequency profiles are based on values from Kelley[48], discussed further in Section 5.2.

This imposes a frequency cutoff on compressional Alfvén waves which scales with the azimuthal modenumber, as shown in Figure 4.1. At small values of m , most of the magnetosphere is conducive to compressional Alfvén waves in the Pc4 frequency range. As m increases, and the wave vector with it, the inner magnetosphere becomes increasingly inaccessible to them.

Chapter 5

“Tuna Half” Dimensional Model

The present section describes the implementation of Tuna, a new two and a half dimensional Alfvén wave code based largely on work by Lysak[59, 62].

The half-integer dimensionality refers to the fact that Tuna’s spatial grid resolves a two-dimensional slice of the magnetosphere, but that electric and magnetic fields — as well as their curls — are three-dimensional vectors. This apparent contradiction is reconciled by the use of a fixed azimuthal modenumber, m . Electric and magnetic fields are taken to be complex-valued, varying azimuthally per $\exp(im\phi)$; derivatives with respect to ϕ are then replaced by a factor of im .

Unlike a fully three-dimensional code, Tuna cannot resolve the evolution of wave structures in the azimuthal direction. Furthermore, the model does not allow coupling between the dayside and nightside magnetospheres. What Tuna does offer is efficiency. The model’s economical geometry allows it to include a realistic Earthward boundary: grid spacing on the order of 10 km, a height-resolved ionospheric conductivity tensor, and even the computation of magnetic field signatures at the ground. Such features are computationally infeasible for a large global code.

Tuna was developed with field line resonance in mind. As discussed in Chapter 3, such waves are azimuthally localized, minimizing the importance of Tuna’s missing half dimension. Moreover, because field line resonances are known to be affected by both

the ionosphere and the plasmasphere, a faithful treatment of the inner magnetosphere is a crucial part of studying them numerically.

Perhaps the most exciting feature of Tuna is its novel driving mechanism: ring current perturbation. Codes similar to Tuna have traditionally been driven using compressional pulses at the outer boundary[59, 62, 101, 102]. This has precluded the investigation of waves with large azimuthal modenumber — such as giant pulsations — which are guided, and thus must be driven from within the magnetosphere.

TODO: The dipole geometry isn't super new, but it's not widely used. The height-resolved ionosphere is new and exciting! Ground signatures are new and exciting!

TODO: The support software — the driver and the plotter — are also significant. Do they get mentioned here? Does the Git repository where the code can be accessed get mentioned here?

5.1 Coordinate System

Field line resonance has traditionally been modeled by straightening the field lines into a rectangular configuration[22, 65], by unrolling the azimuthal coordinate into a cylindrical coordinate system[80], or through the use of dipole coordinates[79]¹:

$$x \equiv -\frac{\sin^2 \theta}{r} \quad y \equiv \phi \quad z \equiv \frac{\cos \theta}{r^2} \quad (5.1)$$

Where r , θ , and ϕ take on their usual spherical meanings of radial distance, colatitude, and azimuthal angle respectively.

The dipole coordinate x is constant over each equipotential shell², y is azimuthal angle, and z indexes each field line from south to north. The unit vectors \hat{x} , \hat{y} , and \hat{z} point

¹The dipole coordinates x , y and z are perhaps more commonly named μ , ϕ , and ν respectively; however, in the present work, μ and ν take other meanings.

²In fact, x is inversely proportional to the McIlwain parameter L .

in the crosswise³ (radially outward at the equator), azimuthal (eastward), and parallel (northward at the equator) directions respectively.

Notably, the dipole coordinates in Equation (5.1) are normal to one another. While mathematically convenient, they do not readily accommodate a fixed-altitude boundary at the ionosphere, nor do they allow the dipole magnetic field to intersect the boundary at an oblique angle, as Earth's field does. As a solution, a nonorthogonal set of dipole coordinates was developed numerically by Proehl[78], then formalized analytically by Lysak[59] in terms of their contravariant components:

$$u^1 = -\frac{R_I}{r} \sin^2 \theta \quad u^2 = \phi \quad u^3 = \frac{R_I^2}{r^2} \frac{\cos \theta}{\cos \theta_0} \quad (5.2)$$

Above, R_I is the position of the ionosphere relative to Earth's center; it's typically taken to be $1 R_E + 100 \text{ km}$.

Like the dipole coordinates x , y , and z , Lysak's coordinates u^1 , u^2 , and u^3 correspond to L -shell, azimuthal angle, and position along a field line respectively. However, compared to z , u^3 has been renormalized using the invariant colatitude⁴ θ_0 . As a result, u^3 takes the value $+1$ at the northern ionospheric boundary and -1 at the southern ionospheric boundary for all field lines.

Because Lysak's coordinate system is not orthogonal⁵, it's necessary to consider covariant and contravariant basis vectors separately.

$$\hat{e}_i \equiv \frac{\partial}{\partial u^i} \underline{x} \quad \hat{e}^i \equiv \frac{\partial}{\partial \underline{x}} u^i \quad (5.3)$$

Covariant basis vectors \hat{e}_i are normal to the curve defined by constant u^i , while contravariant basis vectors \hat{e}^i are tangent to the coordinate curve (equivalently, \hat{e}^i is normal

³In the context of in situ measurements taken near the equatorial plane, \hat{x} is referred to as the radial direction; however, the present work extends the dipole grid to low altitudes, where \hat{x} can be more horizontal than vertical. The term "crosswise" is meant to indicate that \hat{x} is defined by the cross product of \hat{y} and \hat{z} .

⁴The invariant colatitude is the colatitude θ at which a field line intersects the ionosphere. It is related to the McIlwain parameter by $\cos \theta_0 \equiv \sqrt{1 - \frac{R_I}{L}}$.

⁵Curves of constant u^1 and curves of constant u^3 can intersect at non-right angles.

to the plane defined by constant u^j for all $j \neq i$). These vectors are reciprocal⁶ to one another, and can be combined to give components of the metric tensor $\underline{\underline{g}}$ [20].

$$\hat{e}^i \cdot \hat{e}_j = \delta_j^i \quad g_{ij} \equiv \hat{e}_i \cdot \hat{e}_j \quad g^{ij} \equiv \hat{e}^i \cdot \hat{e}^j \quad (5.4)$$

The metric tensor allows rotation between covariant and contravariant representations of vectors.

$$A_i = g_{ij} A^j \quad \text{and} \quad A^i = g^{ij} A_j \quad \text{where} \quad A_i \equiv \underline{A} \cdot \hat{e}_i \quad \text{and} \quad A^i \equiv \underline{A} \cdot \hat{e}^i \quad (5.5)$$

In addition, the determinant of the metric tensor is used to define cross products and curls⁷.

$$(\underline{A} \times \underline{B})^i = \frac{\varepsilon^{ijk}}{\sqrt{g}} A_j B_k \quad \text{and} \quad (\nabla \times \underline{A})^i = \frac{\varepsilon^{ijk}}{\sqrt{g}} \frac{\partial}{\partial u^j} A_k \quad \text{where} \quad g \equiv \det \underline{\underline{g}} \quad (5.6)$$

Explicit forms of the basis vectors and metric tensor can be found in the appendix of Lysak's 2004 paper[59]. At present, it's sufficient to note the mapping between Lysak's basis vectors and the usual dipole unit vectors.

$$\hat{x} = \frac{1}{\sqrt{g^{11}}} \hat{e}^1 \quad \hat{y} = \frac{1}{\sqrt{g^{22}}} \hat{e}^2 \quad \hat{z} = \frac{1}{\sqrt{g^{33}}} \hat{e}^3 \quad (5.7)$$

TODO: Do these need to be written out? Referring people to the code, which will be in a public Git repository, is also a possibility.

The basis vectors can also be mapped to the spherical unit vectors, though Equation (5.8) is valid only at the ionospheric boundary.

$$\hat{\theta} = \frac{1}{\sqrt{g_{11}}} \hat{e}_1 \quad \hat{\phi} = \frac{1}{\sqrt{g_{22}}} \hat{e}_2 \quad \hat{r} = \frac{1}{\sqrt{g_{33}}} \hat{e}_3 \quad (5.8)$$

⁶The symbol δ_j^i is the Kronecker delta; the present work also makes use of the Levi-Civita symbol ε^{ijk} and Einstein's convention of implied summation over repeated indeces[24].

⁷The square root of the determinant of the metric tensor is called the Jacobian. It's sometimes denoted using the letter J , which is reserved for current in the present work.

The coordinates converge at the equatorial ionosphere, so an inner boundary is necessary to maintain finite grid spacing. It's typically placed at $L = 2$. The outer boundary is at $L = 10$. The dipole approximation of Earth's magnetic field is tenuous at the outer boundary (particularly on the dayside); however, in practice, wave activity is localized inside $L \sim 7$. The grid is spaced uniformly in u^1 , which gives finer resolution close to Earth and coarser resolution at large distances.

Spacing in u^3 is set by placing grid points along the outermost field line. The points are closest together at the ionosphere, and grow towards the equator. The spacing increases in a geometric fashion, typically by 3%.

Typically, Tuna uses a grid 150 points in u^1 by 350 points in u^3 . The result is a resolution on the order of 10 km at the ionosphere, which increases to the order of 10³ km at the midpoint of the outermost field line.

There are no grid points in u^2 due to the two-and-a-half-dimensional nature of the model. Fields are assumed to vary as $\exp(imu^2)$ — equally, $\exp(im\phi)$ — so derivatives with respect to u^2 are equivalent to a factor of im . In effect, the real component of each field is azimuthally in phase with the (purely real) driving, while imaginary values represent behavior that is azimuthally offset.

The simulation's time step is set based on the grid spacing. As is the convention, δt is set to match the smallest Alfvén zone crossing time, scaled down by a Courant factor (typically 0.1). It bears noting that the smallest crossing time need not correspond to the smallest zone; the Alfvén speed peaks several thousand kilometers above Earth's surface, in the so-called Ionospheric Alfvén Resonator[62]. A typical time step is on the order of 10⁻⁵ s.

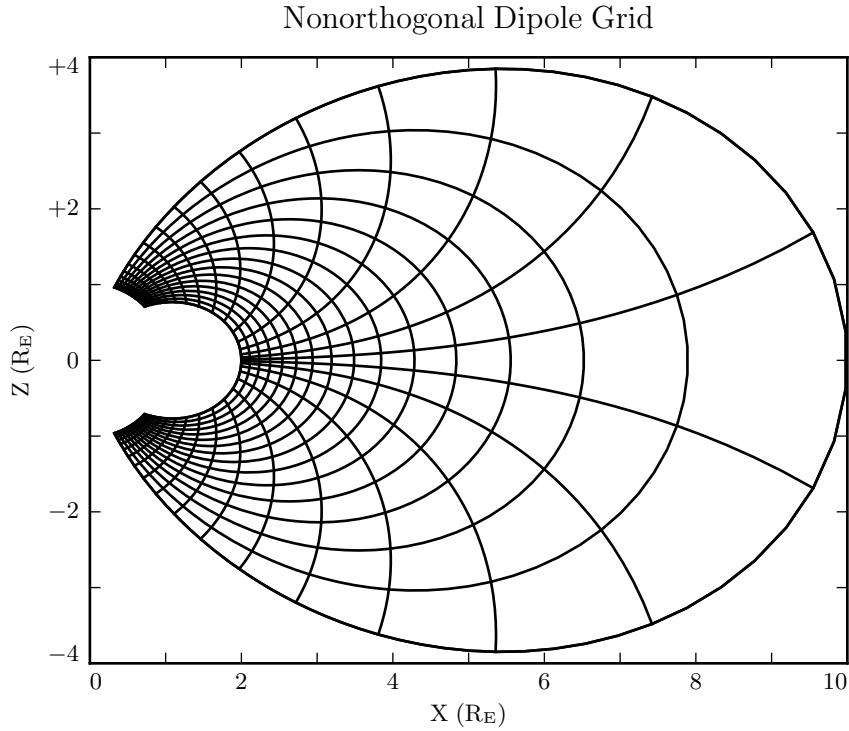


Figure 5.1: The model’s nonorthogonal dipole grid. Every fifth point is shown in each direction. The high concentration of grid points near Earth’s equator is a consequence of the coordinate system, which converges at the equatorial ionosphere. Earth (not shown) is centered at the origin with unit radius.

5.2 Physical Parameter Profiles

Tuna models Earth’s magnetic field to be an ideal dipole, so the zeroth-order field strength is written in the usual form:

$$\underline{B}_0 = 3.1 \times 10^4 \text{ nT} \left(\frac{R_E}{r} \right)^3 \left(2 \cos \theta \hat{r} - \sin \theta \hat{\theta} \right) \quad (5.9)$$

Number density is taken to be the sum of an inverse-radial-dependent auroral profile and a plasmaspheric profile dependent on the L -shell[62]:

$$n = n_{AZ} \frac{r_{AZ}}{r} + n_{PS} \exp\left(\frac{-L}{L_{PS}}\right) \left(\frac{1}{2} - \frac{1}{2} \tanh \frac{L - L_{PP}}{\delta L_{PP}} \right) \quad (5.10)$$

Where typical values are shown in Table 5.1.

Table 5.1: Typical Parameters for the Tuna Density Profile

Variable	Value	Description
L_{PS}	1.1	Scale L of the plasmasphere.
L_{PP}	4.0	Location of the plasmapause.
δL_{PP}	0.1	Thickness of the plasmapause.
n_{AZ}	$10 / \text{cm}^3$	Number density at the base of the auroral zone.
n_{PS}	$10^4 / \text{cm}^3$	Number density at the base of the plasmasphere.
r_{AZ}	1 R_E	Scale height of the auroral density distribution.

The perpendicular component of the electric tensor, ϵ_{\perp} , is computed based on Kelley's[48] tabulated low-density values, ϵ_K , which are adjusted to take into account the effects of high density in the plasmapause.

$$\epsilon_{\perp} = \epsilon_K + \frac{Mn}{B_0^2} \quad (5.11)$$

Where M is the mean molecular mass, which is large ($\sim 28 \text{ u}$) at 100 km altitude, then drops quickly (down to 1 u by $\sim 1000 \text{ km}$)[62].

The Alfvén speed profile is computed from the perpendicular electric constant in the usual way, $v_A^2 \equiv \frac{1}{\mu_0 \epsilon_{\perp}}$. This form takes into account the effect of the displacement current, which becomes important in regions where the Alfvén speed approaches the speed of light.

While the density profile is held constant for all runs discussed in the present work, the Alfvén speed profile is not. Four different profiles are used for the low-density

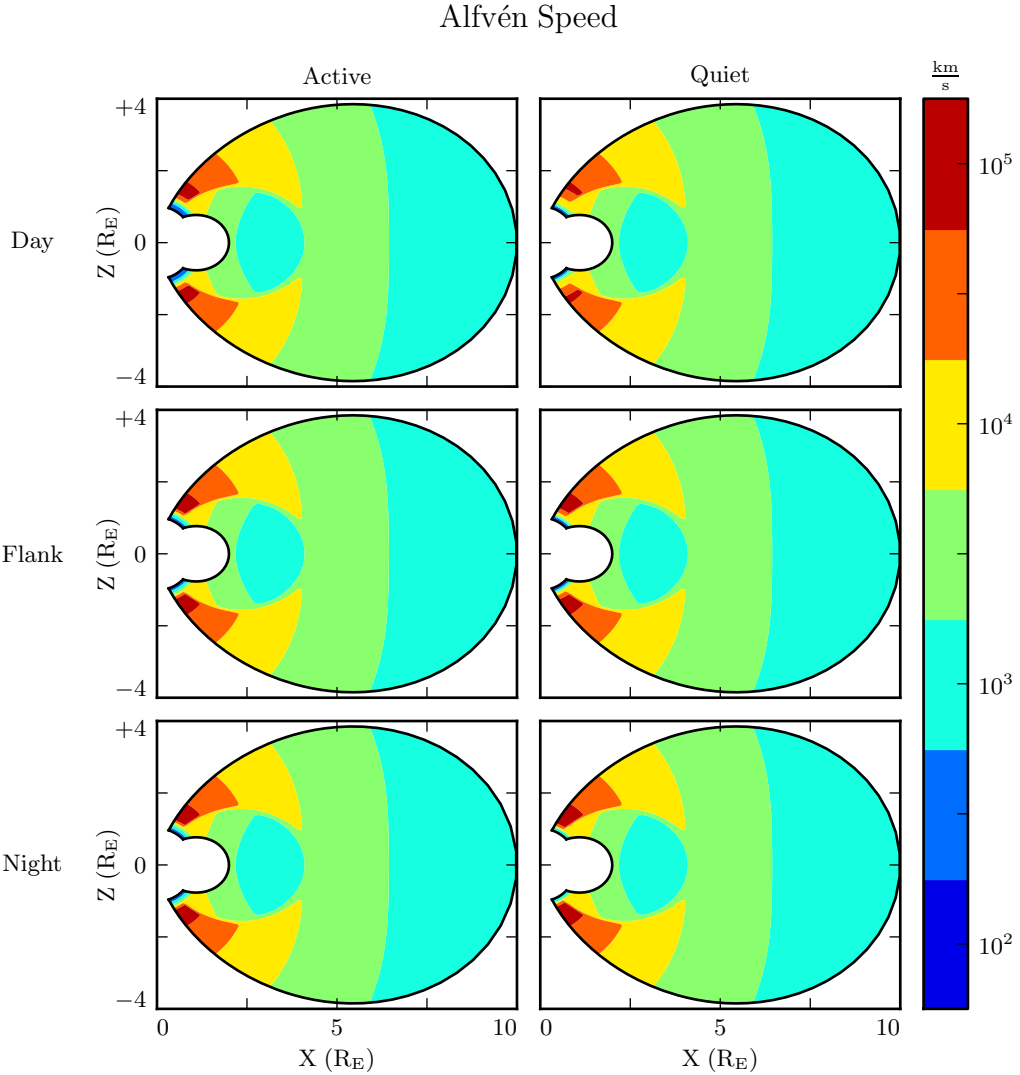


Figure 5.2: Alfvén speed profiles are based on low-density values tabulated by Kelley[48]. They are adjusted to take into account the density of the plasmapause and mass loading near the Earthward boundary.

perpendicular electric constant ϵ_K , corresponding to the differing ionospheric conditions between the dayside and the nightside, and between the high and low points in the solar cycle. These differences are visible in Figure 5.2, particularly in the size of the ionospheric Alfvén resonator (the peak in Alfvén speed in the high-latitude ionosphere).

TODO: Runs are only carried out for day and night... is it even worth showing the flank profile?

Pedersen (Blue), Hall (Red), and Parallel (Green) Conductivities

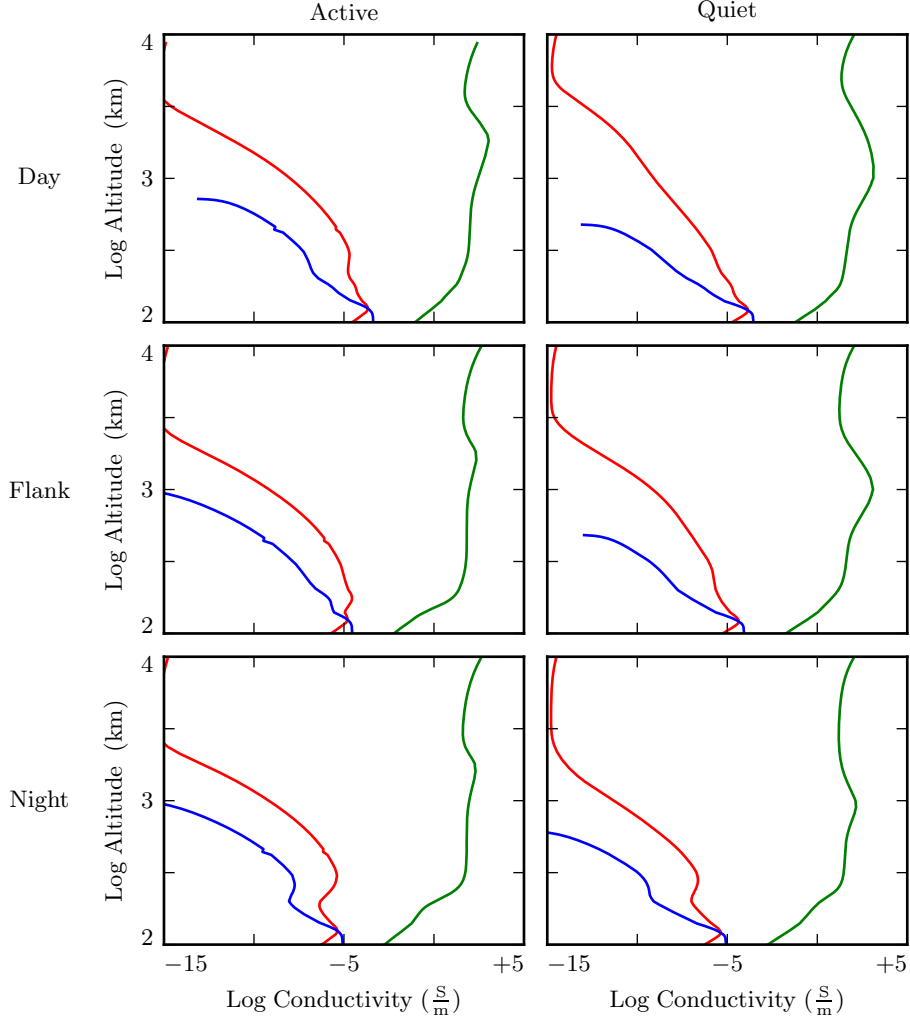


Figure 5.3: Ionospheric conductivity profiles are adapted by Lysak[62] from Kelley's tabulated values[48]. These profiles allow Tuna to simulate magnetosphere-ionosphere coupling under a variety of conditions.

Ionospheric conductivity profiles are also based on values tabulated by Kelley, adjusted by Lysak[62] to take into account the abundance of heavy ions near the Earthward

boundary. Pedersen, Hall, and parallel conductivities are each resolved by altitude, as shown in Figure 5.3.

Tuna’s physical parameter profiles are static over the course of each run. Even so-called ultra low frequency waves like Pc4 pulsations are fast compared to convective timescales in the magnetosphere.

5.3 Driving

Models similar to Tuna have traditionally been driven using compression at the outer boundary[59, 62, 101, 102]. Such driving acts as a proxy for solar wind compression, Kelvin-Helmholtz effects at the magnetopause, and so on. However, because of the constraints imposed by the dispersion relation for Alfvén waves⁸, simulations driven from the outer boundary are constrained to the consideration of waves with low azimuthal modenumber (equivalently, large azimuthal wavelength).

This issue is demonstrated in Figure 5.4. At low modenumber, energy delivered at the outer boundary propagates across field lines in order to stimulate resonances in the inner magnetosphere. However, as modenumber increases, Alfvén waves become increasingly guided, and the inner magnetosphere is unaffected by perturbations at the outer boundary.

In order to simulate high-modenumber Alfvén waves in the inner magnetosphere — such as giant pulsations — a new driving mechanism is necessary. Perturbation of the ring current is a natural choice, as Alfvén waves in the Pc4 range are known to interact with ring current particles through drift and drift-bounce resonances. The ring current is a dynamic region, particularly during and after geomagnetic storms; it’s easy to imagine the formation of localized inhomogeneities.

In order to estimate an appropriate magnitude for perturbations of the ring current, the Sym-H storm index is used. The index is measured once per minute, and so cannot

⁸See Section 4.4.

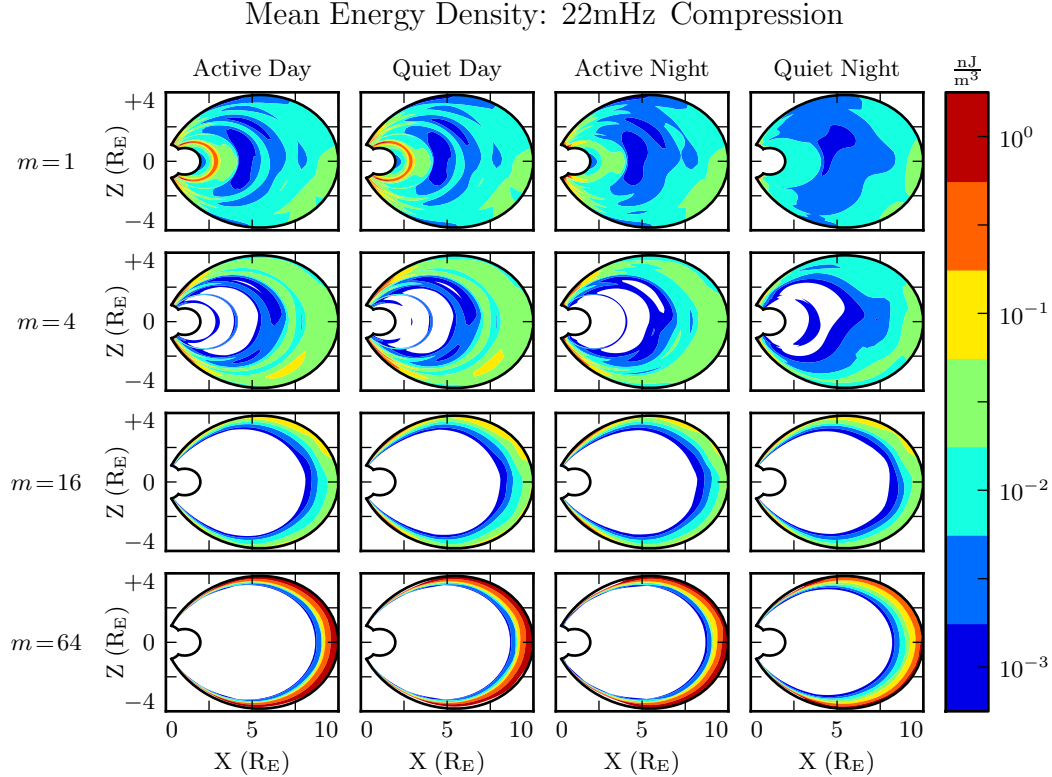


Figure 5.4: Each cell presents the mean energy density over the course of a 300 s run, as a function of position, due to compressional driving at the outer boundary. Azimuthal modenumber varies by row, and ionospheric conditions vary by column. For runs with small azimuthal modenumber, it's clear that energy is able to propagate across field lines and stimulate wave activity in the inner magnetosphere. When the modenumber is large, energy is unable to penetrate to the inner magnetosphere. Notably, the large values on the bottom row should be taken with a grain of salt; it's not clear that the model's results are reliable when waves are continuously forced against the boundary.

directly detect ring current modulations in the Pc4 frequency range. Instead, the index is transformed into the frequency domain, allowing a fit of its pink noise⁹.

As shown in Figure 5.5, a Fourier transform of the Sym-H index (taken here from the June 2013 storm) suggests that magnetic field perturbations at Earth's surface due to

⁹Pink noise, also called $\frac{1}{f}$ noise, refers to the power law decay present in the Fourier transforms of all manner of physical signals.

ring current activity in the Pc4 frequency range could be up to the order of 10^{-2} nT. Supposing that the ring current is centered around $5 R_E$ geocentric, that corresponds to a current on the order of 0.1 MA. Tuna's driving is spread using a Gaussian profile in u^1 (typically centered at $L = 5$) and u^3 (typically centered just off the equator), with a characteristic area of $1 R_E^2$; this gives a current density on the order of $10^{-4} \mu\text{A}/\text{m}^2$.

TODO: Admittedly, estimating the strength of localized perturbations using Sym-H — an index averaged over the entire globe — is a bit of a kludge.

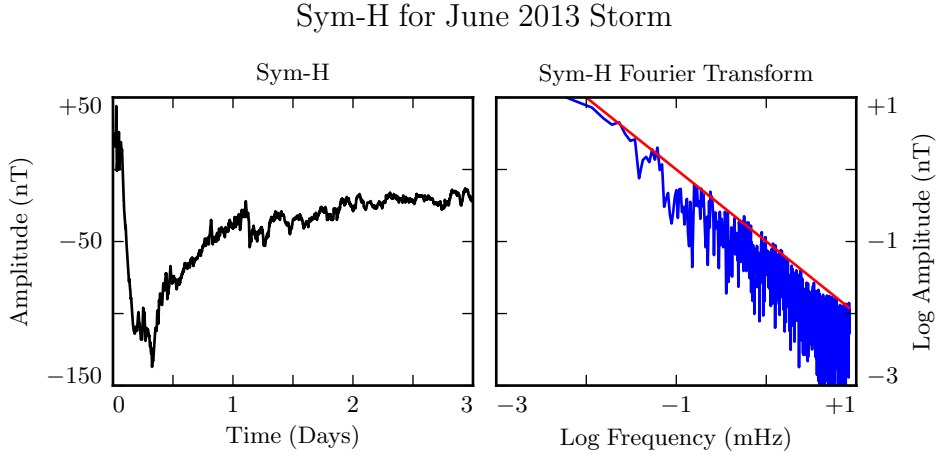


Figure 5.5: The Sym-H storm index[72] measures magnetic perturbations on Earth's surface due to ring current activity. The amplitude of oscillations in the Pc4 range is estimated by fitting the pink noise in its Fourier transform.

In situ observations of Pc4 pulsations and giant pulsations have shown waves with modenumbers across the range $1 \lesssim m \lesssim 100$ [17, 18, 92]. Simulations are carried out across that range, corresponding to ring current perturbations with azimuthal extent as small as $0.5 R_E$.

TODO: Driving is delivered in the azimuthal component of the current only.

TODO: Driving is sinusoidal.

TODO: In case it's not clear: Chapter 7 discusses ONLY simulations using ring current driving. The only compressional driving we look at is Figure 5.4.

5.4 Maxwell's Equations

Tuna simulates the evolution of electromagnetic waves in accordance with Ampère's law and Faraday's law. Computation is carried out on a Yee grid[106]: electric fields and magnetic fields are offset by half a time step, and each field component is defined on either odd or even grid points in each dimension to ensure that curls are computed using centered differences.

The Ohmic current in Ampère's law is replaced with $\underline{\sigma} \cdot \underline{E}$ per Kirchhoff's formulation of Ohm's law. Then, taking \underline{J} to represent the driving current discussed in Section 5.3, Maxwell's equations can be written

$$\frac{\partial}{\partial t} \underline{B} = -\nabla \times \underline{E} \quad \underline{\epsilon} \cdot \frac{\partial}{\partial t} \underline{E} = \frac{1}{\mu_0} \nabla \times \underline{B} - \underline{J} - \underline{\sigma} \cdot \underline{E} \quad (5.12)$$

It is convenient to introduce shorthand for the curl of each field: $\underline{C} \equiv \nabla \times \underline{E}$ and $\underline{F} \equiv \nabla \times \underline{B} - \mu_0 \underline{J}$. Or, recalling Equation (5.6),

$$C^i = \frac{\varepsilon^{ijk}}{\sqrt{g}} \frac{\partial}{\partial u^j} E_k \quad F^i = \frac{\varepsilon^{ijk}}{\sqrt{g}} \frac{\partial}{\partial u^j} B_k - J^i \quad (5.13)$$

In these terms, Faraday's law can simply be written:

$$\frac{\partial}{\partial t} B^i = -C^i \quad (5.14)$$

Writing each component out explicitly, and using the metric tensor (per Equation (5.5)) to eliminate contravariant magnetic field components¹⁰, Equation (5.14) becomes:

$$\begin{aligned} B_1 &\leftarrow B_1 - g_{11} \delta t C^1 - g_{13} \delta t C^3 \\ B_2 &\leftarrow B_2 - g_{22} \delta t C^2 \\ B_3 &\leftarrow B_3 - g_{31} \delta t C^1 - g_{33} \delta t C^3 \end{aligned} \quad (5.15)$$

Note that the \leftarrow operator is used in Equation (5.15) to indicate assignment, rather than equality. Terms on the left are new, while those on the right are old.

Unlike Faraday's law, Ampère's law cannot be trivially solved. Not only does the derivative of \underline{E} depend on its own future value, but the crosswise and azimuthal components of the equation are coupled by the Hall terms in the conductivity tensor. Fortunately, the electric tensor can be inverted, allowing a solution by integrating factors:

$$\underline{\epsilon} \cdot \frac{\partial}{\partial t} \underline{E} = \frac{1}{\mu_0} \underline{F} - \underline{\sigma} \cdot \underline{E} \quad \text{becomes} \quad \left(\underline{\Omega} + \underline{\underline{\epsilon}} \frac{\partial}{\partial t} \right) \cdot \underline{E} = \underline{\underline{V}}^2 \cdot \underline{F} \quad (5.16)$$

Where $\underline{\underline{\epsilon}}$ is the identity tensor and in x - y - z coordinates¹¹,

$$\underline{\underline{V}}^2 \equiv \frac{1}{\mu_0} \underline{\underline{\epsilon}}^{-1} = \begin{bmatrix} v_A^2 & 0 & 0 \\ 0 & v_A^2 & 0 \\ 0 & 0 & c^2 \end{bmatrix} \quad \text{and} \quad \underline{\Omega} \equiv \underline{\underline{\epsilon}}^{-1} \cdot \underline{\sigma} = \begin{bmatrix} \frac{\sigma_P}{\epsilon_\perp} & \frac{-\sigma_H}{\epsilon_\perp} & 0 \\ \frac{\sigma_H}{\epsilon_\perp} & \frac{\sigma_P}{\epsilon_\perp} & 0 \\ 0 & 0 & \frac{\sigma_0}{\epsilon_0} \end{bmatrix} \quad (5.17)$$

¹⁰FIELDS are stored only in terms of their covariant components, and CURLS in terms of their contravariant components. This reduces Tuna's memory footprint (since each field need not be stored twice) as well as its computational cost (since time need not be spent rotating between bases). As a result, Tuna's solutions to Maxwell's equations are linear expressions whose coefficients are a mishmash of physical constants and geometric factors. To save time, each coefficient is computed once and stored, rather than being multiplied out from scratch with each time step.

¹¹Note the parallel component of the present definition of $\underline{\Omega}$ differs slightly from that used in Chapter 4, due to the present neglect of inertial effects; see Chapter 6.

Multiplying through by $\exp(\underline{\Omega} t)$ and applying the product rule, Equation (5.16) becomes¹²

$$\frac{\partial}{\partial t} \left(\exp(\underline{\Omega} t) \cdot \underline{E} \right) = \exp(\underline{\Omega} t) \cdot \underline{V}^2 \cdot \underline{F} \quad (5.18)$$

Equation (5.18) can then be integrated over a small time step δt and expressed in terms of the assignment operator introduced in Equation (5.15).

$$\underline{E} \leftarrow \exp(-\underline{\Omega} \delta t) \cdot \underline{E} + \delta t \exp(-\underline{\Omega} \frac{\delta t}{2}) \cdot \underline{V}^2 \cdot \underline{F} \quad (5.19)$$

The tensor exponential can be evaluated by splitting $\underline{\Omega}$ into the sum of its diagonal and Hall components¹³. The Hall exponential condenses into sines and cosines, giving a rotation around the magnetic field line:

$$\underline{E} \leftarrow \exp(-\underline{\Omega}' \delta t) \cdot \underline{R}_z \left(\frac{-\sigma_H \delta t}{\epsilon_{\perp}} \right) \cdot \underline{E} + \delta t \underline{V}^2 \cdot \exp(-\underline{\Omega}' \frac{\delta t}{2}) \cdot \underline{R}_z \left(\frac{-\sigma_H \delta t}{2\epsilon_{\perp}} \right) \cdot \underline{F} \quad (5.20)$$

Where

$$\underline{R}_z(\theta) = \begin{bmatrix} \cos \theta & -\sin \theta & 0 \\ \sin \theta & \cos \theta & 0 \\ 0 & 0 & 1 \end{bmatrix} \quad \text{and} \quad \underline{\Omega}' \equiv \begin{bmatrix} \frac{\sigma_P}{\epsilon_{\perp}} & 0 & 0 \\ 0 & \frac{\sigma_P}{\epsilon_{\perp}} & 0 \\ 0 & 0 & \frac{\sigma_0}{\epsilon_0} \end{bmatrix} \quad (5.21)$$

The parallel component of term of Equation (5.20) is simply

$$E_z \leftarrow E_z \exp\left(\frac{-\sigma_0 \delta t}{\epsilon_0}\right) + c^2 \delta t F_z \exp\left(\frac{-\sigma_0 \delta t}{2\epsilon_0}\right) \quad (5.22)$$

Or, using Equation (5.7) to map to the covariant basis,

$$E_3 \leftarrow E_3 \exp\left(\frac{-\sigma_0 \delta t}{\epsilon_0}\right) + c^2 \delta t (g_{31} F^1 + g_{33} F^3) \exp\left(\frac{-\sigma_0 \delta t}{2\epsilon_0}\right) \quad (5.23)$$

¹²Tensor exponentiation is analogous to scalar exponentiation[38]: $\exp(\underline{T}) \equiv \sum_n \frac{1}{n!} \underline{T}^n$.

¹³For tensors, $\exp(\underline{S} + \underline{T}) = \exp(\underline{S}) \exp(\underline{T})$ as long as $\underline{S} \cdot \underline{T} = \underline{T} \cdot \underline{S}$.

Tuna's conductivity profile gives a minimum value of $\frac{\sigma_0 \delta t}{\epsilon_0}$ on the order of 10^3 , making $\exp\left(\frac{-\sigma_0 \delta t}{\epsilon_0}\right)$ far too small to be stored in a double precision variable¹⁴. That is, this model takes E_3 (and, proportionally, E_z) to be uniformly zero. This issue is revisited in Chapter 6.

The perpendicular components of Equation (5.20) give the expressions:

$$\begin{aligned}
E_1 + \frac{g^{13}}{g^{11}} E_3 &\leftarrow E_1 \cos\left(\frac{-\sigma_H \delta t}{\epsilon_{\perp}}\right) \exp\left(\frac{-\sigma_P \delta t}{\epsilon_{\perp}}\right) \\
&+ E_2 \sin\left(\frac{-\sigma_H \delta t}{\epsilon_{\perp}}\right) \exp\left(\frac{-\sigma_P \delta t}{\epsilon_{\perp}}\right) \sqrt{\frac{g^{22}}{g^{11}}} \\
&+ E_3 \cos\left(\frac{-\sigma_H \delta t}{\epsilon_{\perp}}\right) \exp\left(\frac{-\sigma_P \delta t}{\epsilon_{\perp}}\right) \frac{g^{13}}{g^{11}} \\
&+ F^1 \cos\left(\frac{-\sigma_H \delta t}{2\epsilon_{\perp}}\right) \exp\left(\frac{-\sigma_P \delta t}{2\epsilon_{\perp}}\right) \frac{v_A^2 \delta t}{g^{11}} \\
&+ F^2 \sin\left(\frac{-\sigma_H \delta t}{2\epsilon_{\perp}}\right) \exp\left(\frac{-\sigma_P \delta t}{2\epsilon_{\perp}}\right) \frac{v_A^2 \delta t}{\sqrt{g^{11} g^{22}}}
\end{aligned} \tag{5.24}$$

and

$$\begin{aligned}
E_2 &\leftarrow -E_1 \sin\left(\frac{-\sigma_H \delta t}{\epsilon_{\perp}}\right) \exp\left(\frac{-\sigma_P \delta t}{\epsilon_{\perp}}\right) \sqrt{\frac{g^{11}}{g^{22}}} \\
&+ E_2 \cos\left(\frac{-\sigma_H \delta t}{\epsilon_{\perp}}\right) \exp\left(\frac{-\sigma_P \delta t}{\epsilon_{\perp}}\right) \\
&- E_3 \sin\left(\frac{-\sigma_H \delta t}{\epsilon_{\perp}}\right) \exp\left(\frac{-\sigma_P \delta t}{\epsilon_{\perp}}\right) \frac{g^{13}}{\sqrt{g^{11} g^{22}}} \\
&- F^1 \sin\left(\frac{-\sigma_H \delta t}{2\epsilon_{\perp}}\right) \exp\left(\frac{-\sigma_P \delta t}{2\epsilon_{\perp}}\right) \frac{v_A^2 \delta t}{\sqrt{g^{11} g^{22}}} \\
&+ F^2 \cos\left(\frac{-\sigma_H \delta t}{2\epsilon_{\perp}}\right) \exp\left(\frac{-\sigma_P \delta t}{2\epsilon_{\perp}}\right) \frac{v_A^2 \delta t}{g^{22}}
\end{aligned} \tag{5.25}$$

The E_3 terms in Equations (5.24) and (5.25) can be ignored at present. They are revisited in Chapter 6.

¹⁴Not coincidentally, $\frac{\sigma_0}{\epsilon_0}$ can also be written $\frac{\omega_p^2}{\nu}$. At the ionosphere, the collision frequency ν is fast compared to field line resonance timescales, but it's still slow compared to the plasma frequency.

It bears recalling that the driving current is defined as part of \underline{F} , per Equation (5.13). When the driving current is purely azimuthal ($J^1 = J^3 = 0$), the driving is in principle applied to both the poloidal and the toroidal electric fields through F^2 . However, in practice, the driving applied to the toroidal electric field is vanishingly small. The driving current J^2 is localized around $5 R_E$ geocentric, and $\exp\left(\frac{-\sigma_P \delta t}{2\epsilon_\perp}\right)$ drops off quickly with altitude.

5.5 Boundary Conditions

Dirichlet and Neumann boundary conditions are applied to the electric field components and magnetic field components respectively. That is, electric fields are forced to go to zero at the inner and outer boundaries, and magnetic fields are forced to have a zero derivative normal to the inner and outer boundaries.

These boundary conditions can in principle cause nonphysical reflections at the boundary¹⁵. However, in practice, wave activity is concentrated well within the simulation domain. Simulation results are robust under an exchange of Dirichlet and Neumann boundary conditions (though a self-inconsistent set of boundary conditions, such as applying Neumann boundary conditions to B_1 but Dirichlet boundary conditions to B_3 , quickly causes instability).

The Earthward boundary conditions are as follows.

Between the top of the neutral atmosphere and the bottom of the ionosphere, the model includes a thin, horizontal current sheet representing the ionosphere's E layer[59]. By integrating Ampère's law over the layer, it can be shown[28] that the horizontal electric field values at the edge of the grid are determined by the jump in the horizontal magnetic fields:

$$\underline{\Sigma} \cdot \underline{E} = \frac{1}{\mu_0} \lim_{\delta r \rightarrow 0} \left[\hat{r} \times \underline{B} \right]_{R_I - \delta r}^{R_I + \delta r} \quad (5.26)$$

¹⁵See, for example, the bottom row of Figure 5.4.

The integrated conductivity tensor $\underline{\Sigma}$ can be written in θ - ϕ coordinates as[59]:

$$\underline{\Sigma} \equiv \begin{bmatrix} \frac{\Sigma_0 \Sigma_P}{\Sigma_0 \cos^2 \alpha + \Sigma_P \sin^2 \alpha} & \frac{-\Sigma_0 \Sigma_H}{\Sigma_0 \cos^2 \alpha + \Sigma_P \sin^2 \alpha} \\ \frac{\Sigma_0 \Sigma_H}{\Sigma_0 \cos^2 \alpha + \Sigma_P \sin^2 \alpha} & \Sigma_P + \frac{\Sigma_0^2 \Sigma_H}{\Sigma_0 \cos^2 \alpha + \Sigma_P \sin^2 \alpha} \end{bmatrix} \quad (5.27)$$

Where α is the angle between the magnetic field and the vertical direction, given by $\cos \alpha \equiv \frac{-2 \cos \theta}{\sqrt{1+3 \cos^2 \theta}}$, and Σ_P , Σ_H , and Σ_0 are the height-integrated Pedersen, Hall, and parallel conductivities respectively. Their values are determined by integrating Kelley's[48] conductivity profiles from Earth's surface to the ionospheric boundary; values are shown in Table 5.2.

Table 5.2: Integrated Atmospheric Conductivity (S)

	Σ_0	Σ_P	Σ_H
Active Day	424	0.65	6.03
Quiet Day	284	0.44	4.02
Active Night	9	0.01	0.12
Quiet Night	9	0.01	0.12

An expression for the horizontal electric fields at the boundary can be obtained by inverting Equation (5.26). After mapping to covariant coordinates per Equation (5.8), and taking $\Sigma \equiv \det \underline{\Sigma}$,

$$\begin{aligned} E_1 &\leftarrow \frac{1}{\mu_0 \Sigma} \lim_{\delta r \rightarrow 0} \left[-\Sigma_{\theta\phi} B_1 - \sqrt{\frac{g_{11}}{g_{22}}} \Sigma_{\phi\phi} B_2 \Big|_{R_I-\delta r}^{R_I+\delta r} \right. \\ E_2 &\leftarrow \frac{1}{\mu_0 \Sigma} \lim_{\delta r \rightarrow 0} \left[\sqrt{\frac{g_{22}}{g_{11}}} \Sigma_{\theta\theta} B_1 + \Sigma_{\phi\theta} B_2 \Big|_{R_I-\delta r}^{R_I+\delta r} \right. \end{aligned} \quad (5.28)$$

The atmospheric magnetic field is computed as a linear combination of harmonics. The neutral atmosphere is considered to be a perfect insulator, giving $\nabla \times \underline{B} = 0$. Combined with $\nabla \cdot \underline{B} = 0$ (per Maxwell's equations), this allows the computation of a magnetic scalar potential Ψ such that $\underline{B} = \nabla \Psi$ and Ψ satisfies Laplace's equation, $\nabla^2 \Psi = 0$.

Laplace's equation can be solved analytically; however, a numerical solution is preferable to ensure orthonormality on a discrete and incomplete¹⁶ grid. After separating out the radial and azimuthal dependence in the usual way, the latitudinal component of Laplace's equation can be written in terms of $s \equiv -\sin^2 \theta$:

$$(4s^2 + 4s) \frac{d^2}{ds^2} Y_\ell + (4 + 6s) \frac{d}{ds} Y_\ell - \frac{m^2}{s} Y_\ell = \ell (\ell + 1) Y_\ell \quad (5.29)$$

Using centered differences to linearize the derivatives, Equation (5.29) becomes a system of coupled linear equations, one per field line. It can be solved numerically for eigenvalues ℓ ($\ell + 1$) and eigenfunctions Y_ℓ ¹⁷. In terms of the harmonics Y_ℓ , Ψ between the Earth's surface and the top of the atmosphere can be written

$$\Psi = \sum_\ell \left(a_\ell r^\ell + b_\ell r^{-\ell-1} \right) Y_\ell \quad (5.30)$$

As a boundary condition for Ψ , Earth is assumed to be a perfect conductor. This forces the magnetic field at Earth's surface to be horizontal; that is, $B_r = \frac{\partial}{\partial r} \Psi = 0$. Noting that solutions to Laplace's equation are orthonormal, each element of the sum in Equation (5.30) must be independently zero at R_E . This allows the coefficients a_ℓ and b_ℓ to be expressed in terms of one another.

$$b_\ell = \frac{\ell}{\ell + 1} R_E^{2\ell+1} a_\ell \quad (5.31)$$

The current sheet at the top of the atmosphere is assumed to be horizontal, so the radial component of the magnetic field must be the same just above and just below it. Taking the radial derivative of Equation (5.30) at the top of the atmosphere, and eliminating

¹⁶As discussed in Section 5.1, the grid is constrained to finite L , which excludes the equator as well as the poles.

¹⁷Solving Laplace's equation analytically results in spherical harmonics indexed by both ℓ and m , the separation constants for θ and ϕ respectively. In two and a half dimensions, ϕ is not explicitly resolved, so m is set manually.

b_ℓ with Equation (5.31), gives

$$B_r = \sum_\ell \ell a_\ell R_I^{\ell-1} \left(1 - \lambda^{2\ell+1}\right) Y_\ell \quad \text{where} \quad \lambda \equiv \frac{R_E}{R_I} \sim 0.975 \quad (5.32)$$

The summation can be collapsed by “integrating” over a harmonic¹⁸. Inverse harmonics can be obtained by inverting the eigenvector matrix. Then $Y_\ell \cdot Y_{\ell'}^{-1} = \delta_{\ell\ell'}$ by construction.

$$a_\ell = \frac{1}{\ell R_I^{\ell-1}} \frac{B_r \cdot Y_\ell^{-1}}{1 - \lambda^{2\ell+1}} \quad (5.33)$$

Combining Equations (5.30), (5.31), and (5.33) allows the expression of Ψ at the top and bottom of the atmosphere as a linear combination of radial magnetic field components at the bottom of the ionosphere.

$$\begin{aligned} \Psi_E &= \sum_\ell Y_\ell \frac{R_I}{\ell(\ell-1)} \frac{(2\ell-1)\lambda^\ell}{1-\lambda^{2\ell+1}} B_r \cdot Y_\ell^{-1} \\ \Psi_I &= \sum_\ell Y_\ell \frac{R_I}{\ell(\ell-1)} \frac{(\ell-1)+\ell\lambda^{2\ell+1}}{1-\lambda^{2\ell+1}} B_r \cdot Y_\ell^{-1} \end{aligned} \quad (5.34)$$

Horizontal magnetic fields are obtained by taking derivatives of Ψ .

$$B_1 = \frac{\partial}{\partial u^1} \Psi \quad B_2 = \frac{\partial}{\partial u^2} \Psi \quad (5.35)$$

Horizontal magnetic field values at the top of the atmosphere are used to impose boundary conditions on the electric fields at the bottom of the ionosphere, per Equation (5.28). Those at Earth’s surface are valuable because they allow a direct comparison between model output and ground magnetometer data, after being mapped to physical coordinates per Equation (5.8).

¹⁸Because the functions are defined on a discrete grid, their inner product is not an integral, but a sum: $B_r \cdot Y_\ell^{-1} \equiv \sum_i B_r[i] Y_\ell^{-1}[i]$.

Chapter 6

Electron Inertial Effects

As laid out in Chapter 5, Tuna resolves neither parallel currents nor parallel electric fields. This is unfortunate; parallel electric fields generated by kinetic Alfvén waves (including fundamental field line resonances[81, 97]) are a topic of particular interest in the study of auroral particle precipitation.

Parallel currents and electric fields can be added to Tuna through the consideration of electron inertial effects in Ohm's law:

$$0 = \sigma_0 E_z - J_z \quad \text{becomes} \quad \frac{1}{\nu} \frac{\partial}{\partial t} J_z = \sigma_0 E_z - J_z \quad (6.1)$$

With the addition of the electron inertial term, it is necessary to track the parallel current independent of the parallel electric field¹. Solving by integrating factors² gives

$$J_3 \leftarrow J_3 \exp(-\nu \delta t) + \delta t \frac{ne^2}{m_e} E_3 \exp\left(-\nu \frac{\delta t}{2}\right) \quad (6.2)$$

¹The parallel current J_z is defined on the same points of the Yee grid as E_z . It is offset in time by half of a time step.

²The integrating factors technique is laid out explicitly for Ampère's law in Section 5.4.

From there, the parallel electric field can be updated directly; Equation (5.23) is replaced by the following:

$$E_3 \leftarrow E_3 + c^2 \delta t (g_{31} F^1 + g_{33} F^3) - \frac{\delta t}{\epsilon_0} J_3 \quad (6.3)$$

The present section explores the complications that arise from the addition of the electron inertial term to Ohm's law, as well as a few results that may be gleaned despite those complications. Notably — for reasons discussed in Section 6.3 — the results presented in Chapter 7 do not make use of the electron inertial term.

6.1 The Boris Factor

With the addition of the electron inertial term, a cyclical dependence appears between Ampère's law and Ohm's law:

$$\frac{\partial}{\partial t} E_z \sim -\frac{1}{\epsilon_0} J_z \quad \text{and} \quad \frac{\partial}{\partial t} J_z \sim \frac{n e^2}{m_e} E_z \quad \text{so} \quad \frac{\partial^2}{\partial t^2} E_z \sim -\omega_P^2 E_z \quad (6.4)$$

That is, electron inertial effects come hand in hand with the plasma oscillation.

As mentioned in Chapter 4 and shown in Figure 6.1, plasma oscillation is quite fast — several orders of magnitude smaller than Tuna's time step as determined in Section 5.1 ($\sim 10 \mu\text{s}$). This poses a conundrum. At Tuna's usual time step, the plasma oscillation becomes unstable within seconds³. On the other hand, reducing the time step by three orders of magnitude to resolve the plasma oscillation is computationally infeasible; a run slated for an hour would require six weeks to complete.

As it happens, this problem can be solved by artificially increasing the parallel electric constant above its usual value of ϵ_0 . Doing so lowers both the speed of light and the plasma frequency within the simulation.

This technique — and others like it — has been widespread in numerical modeling since it was presented by Boris in 1970[6]. More recently, Lysak and Song considered its use

³For stability, $\omega_P \delta t < 1$ is necessary.

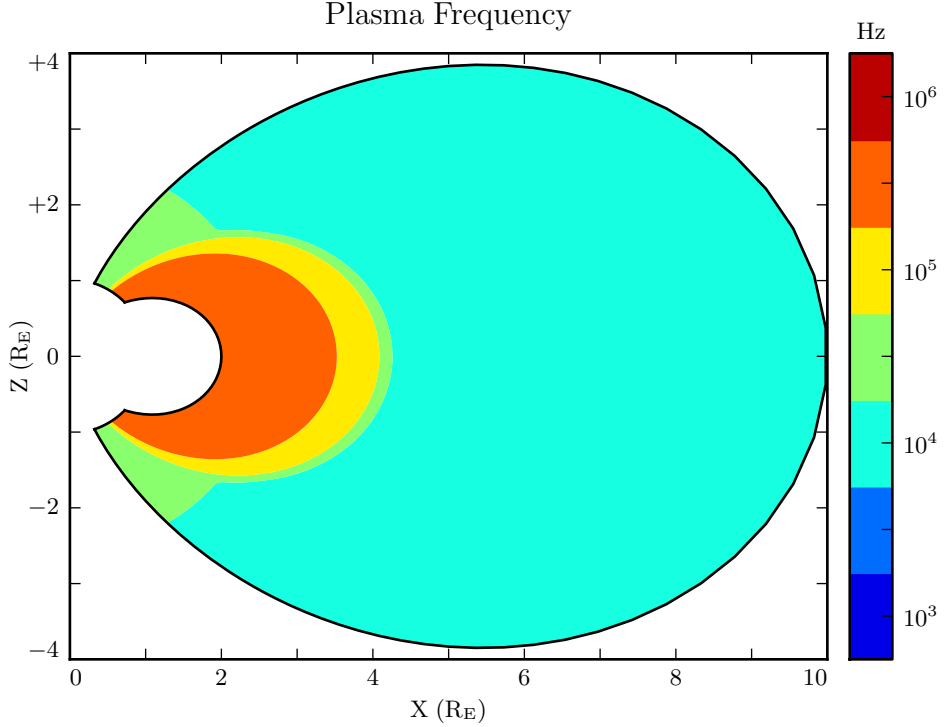


Figure 6.1: The plasma frequency reaches a peak value just under 10^6 Hz near the equator. Outside the plasmasphere, its value is closer to 10^4 Hz, which is still not well-resolved by Tuna's usual time step.

specifically for the case of electron inertial effects[61]. The following paraphrases their argument.

Supposing that the current and electric field are oscillating at frequency ω , the parallel components of Ampère's law and Ohm's law can be written

$$-i\omega\epsilon_0 E_z = \frac{1}{\mu_0} (\nabla \times \underline{B})_z - J_z \quad -\frac{i\omega}{\nu} J_z = \sigma_0 E_z - J_z \quad (6.5)$$

Then, eliminating the current, the parallel electric field can be related to the curl of the magnetic field by⁴

$$\left(1 - \frac{\omega^2 - i\nu\omega}{\omega_P^2}\right) E_z = \frac{c^2}{\omega_P^2} (\nu - i\omega) (\nabla \times \underline{B})_z \quad (6.6)$$

In Equation (6.6), $\frac{c}{\omega_P}$ is the electron inertial length. While the speed of light and the plasma frequency each depend on ϵ_0 , their ratio does not. This allows an estimation of how much the model should be affected by an artificially-large electric constant (and thus an artificially-small plasma frequency): so long as $\frac{\omega^2 - i\nu\omega}{\omega_P^2}$ remains small compared to unity, the model should behave faithfully.

For waves with periods of a minute or so, even perhaps-implausibly large Boris factors are allowed; for example, increasing ϵ_0 by a factor of 10^6 gives $\left|\frac{\omega^2 + i\omega\nu}{\omega_P^2}\right| \lesssim 0.01$.

6.2 Parallel Currents and Electric Fields

As discussed in Section 4.4, parallel electric fields in this regime are expected to be six or more orders of magnitude smaller than the perpendicular electric fields. Numerical results show general agreement: in Figure 6.2, the parallel electric field appears comparable to its perpendicular counterparts only after its been scaled up by six orders of magnitude.

As such, the inclusion of electron inertial effects does not appreciably impact the simulation's gross behavior; in Faraday's law, $\nabla \times \underline{E}$ is essentially unaffected. Side by side snapshots of the magnetic fields in runs carried out with and without electron inertial effects are not visibly distinguishable⁵

Even if there is no significant feedback through Faraday's law, it's informative to consider the structures that arise in parallel currents and electric fields driven by perturbations in the ring current.

⁴From Equation (4.4), $c^2 \equiv \frac{1}{\mu_0 \epsilon_0}$ and $\sigma_0 \equiv \frac{ne^2}{m_e \nu}$ and $\omega_P^2 \equiv \frac{ne^2}{m_e \epsilon_0}$.

⁵In a sense, this is reassuring. It ensures that the present section does not cast doubt on the results presented in Chapter 7, where electron inertial effects are neglected.

Electric Field Snapshots: Quiet Day, 10mHz Current, $m = 16$

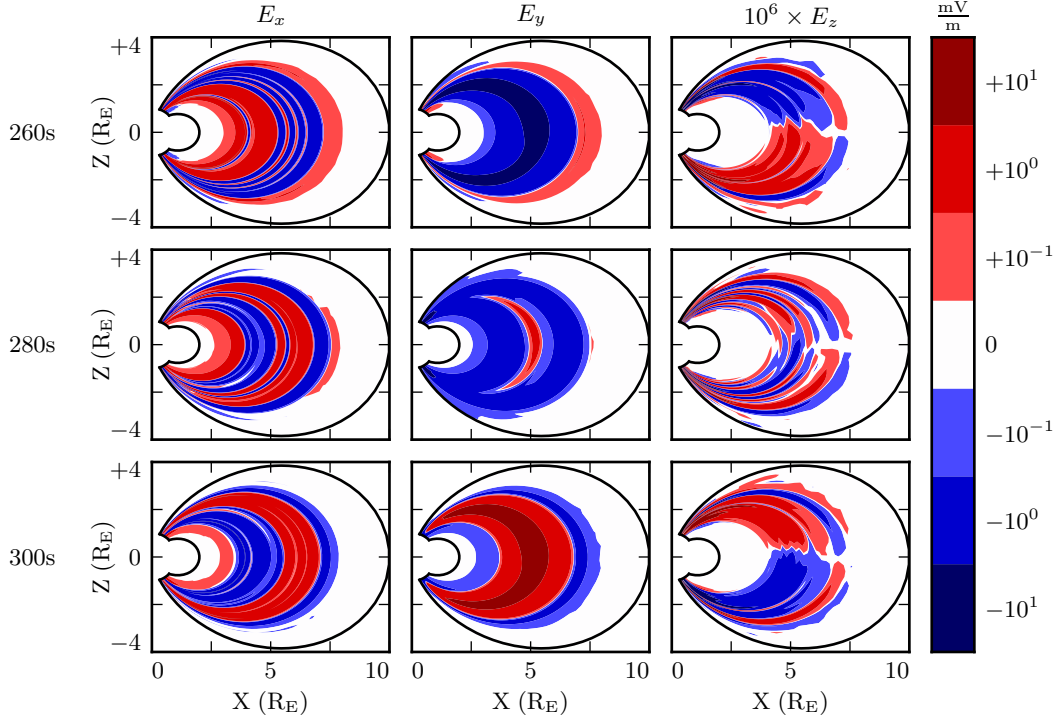


Figure 6.2: Parallel electric fields are smaller than perpendicular electric fields by about six orders of magnitude. As a result, parallel electric fields do not contribute significantly to $\nabla \times \underline{E}$ in Faraday's law.

For example, the parallel electric field is at its maximum value in the ionosphere. This makes its structure qualitatively resemble the Poynting flux than the perpendicular electric field components.

It is furthermore notable that the parallel electric field (and the parallel current that comes from it) exhibits real and imaginary components of comparable magnitude.

TODO: In Figure 6.3, parallel currents top out around $1 \mu\text{A}/\text{m}^2$. This falls about an order of magnitude shy of the up-to-tens of $\mu\text{A}/\text{m}^2$ inferred from ground observations and seen in situ[84, 8, 46].

Current and Poynting Flux at R_I : Active Day , 16mHz Current

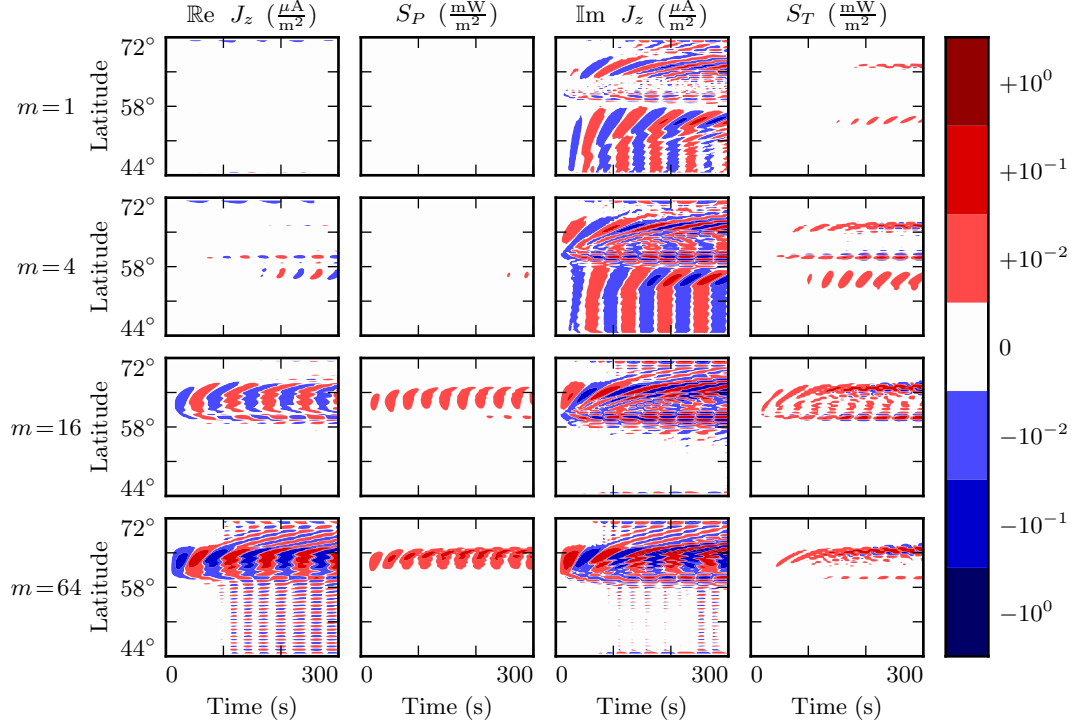


Figure 6.3: Perhaps unsurprisingly, field-aligned current structures at the ionospheric boundary line up with Poynting flux structures. The imaginary component of the current lines up with the toroidal Poynting flux (which is the product of imaginary E_x and imaginary B_y^*), while the real current lines up with the poloidal Poynting flux (E_y and B_x^* are real).

As mentioned in Chapter 5, each field's real component gives its behavior in the meridional plane where the (real) driving is delivered, while imaginary components are representative of waves offset in the azimuthal direction. The Hall conductivity in the ionosphere muddles this relationship somewhat by directly coupling the perpendicular electric field components to one another; even so, the poloidal field components (B_x , E_y , and B_z) are overwhelmingly real while toroidal components (E_x and B_y) are overwhelmingly imaginary.

The parallel electric field and current defy this pattern. The real current scales more or less proportionally with the poloidal Poynting flux, and its imaginary component scales comparably with the toroidal Poynting flux. Rather than being preferentially coupled to one mode or the other, parallel currents seem to arise wherever energy is moving along the background magnetic field.

It bears noting further that the Poynting flux waveforms are rectified — they primarily carry energy Earthward. The current, on the other hand, alternates between upward and downward flow. This effect presumably arises because the current is a linear quantity while the Poynting flux is quadratic: the electric and magnetic fields that make it up oscillate in phase, so their product is positive even when they are negative.

It's also possible to consider the effect of parallel currents and electric fields on the ionosphere's energy budget, per Poynting's theorem:

$$-\frac{\partial}{\partial t}u = \nabla \cdot \underline{E} + \underline{J} \cdot \underline{E} \quad (6.7)$$

As shown in Figure 6.4, little energy transfer in the ionosphere is mediated by perpendicular components of the Poynting flux. The parallel component of $\underline{J} \cdot \underline{E}$ is comparably unimportant. The energy deposited in the ionosphere by the Poynting flux matches closely with the energy lost to Joule dissipation — as it should, to conserve energy — but according to the model, parallel currents and electric fields do not contribute significantly.

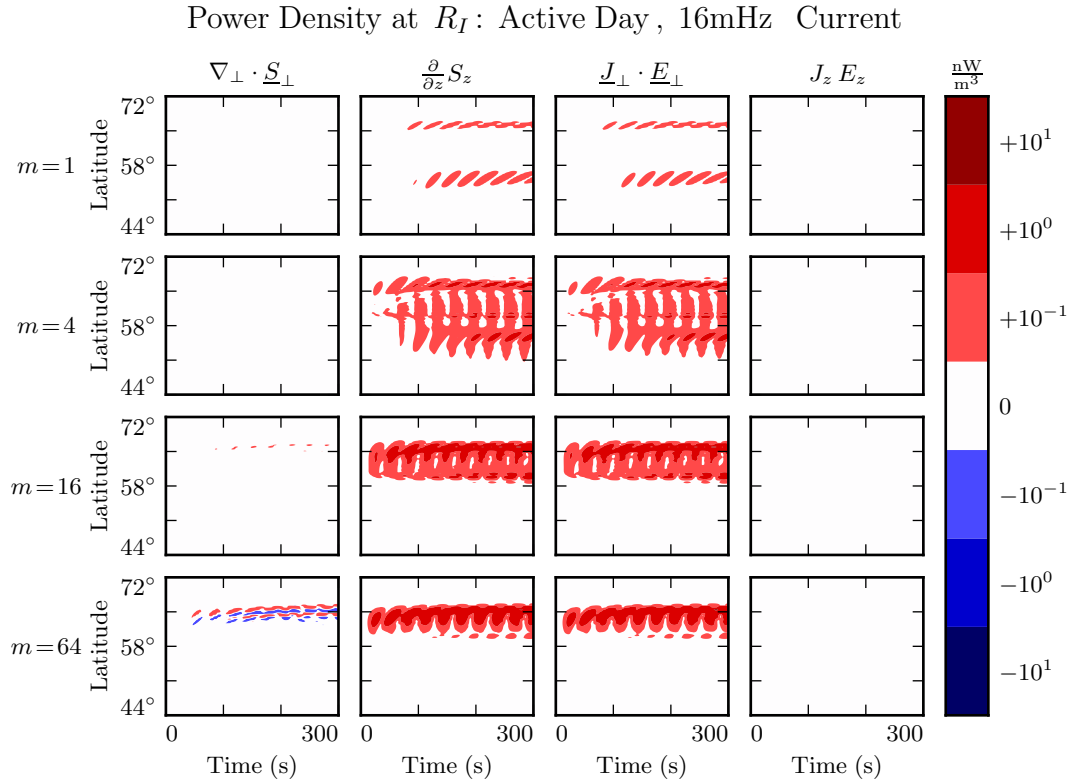


Figure 6.4: While field-aligned currents can be of significant size, they are not particularly good at depositing energy in the ionosphere. Energy deposited by the Poynting flux matches closely with Joule dissipation from the perpendicular currents, while $J_z E_z$ is smaller by several orders of magnitude.

6.3 Inertial Length Scales

It's not quite fair to compare the parallel and perpendicular contributions to $\nabla \times \underline{E}$ as was done in the previous section. Perpendicular electric fields are on the order of 1 mV/m, with wavelengths on the order of 10^5 km; they give rise to magnetic field gradients around 0.1 nT/s. Parallel electric fields, closer to 10^{-6} mV/m, would need to vary over length scales of 0.1 km to match with that.

Such scales are believable. The characteristic length scale of the plasma oscillation is the electron inertial length, $\frac{c}{\omega_p}$, which is on the order of 1 km in the auroral ionosphere

and 0.1 km in the low-altitude plasmasphere. However, such lengths are not resolved by Tuna’s usual grid; its resolution bottoms out closer to 10 km.

That is, with the inclusion of electron inertial effects, Tuna’s grid is not sufficiently fine to resolve all of the waves expected to be present. The model is prone to instability as a result; see, for example, the “wiggles” in the bottom row of Figure 6.3 (in the previous section).

Figure 6.5 shows a run with perpendicular resolution smaller than the electron inertial length, side by side with an analogous run on the usual grid. In order to carry out the inertial-scale run, several concessions were made to computational cost. The run simulates only a duration of 100 s (other results in previous sections and in Chapter 7 show 300 s), and the grid covers only the auroral latitudes from $L = 5$ to $L = 7$.

Parallel Electric Fields: Quiet Day, 100s of 16mHz Current, $m = 16$

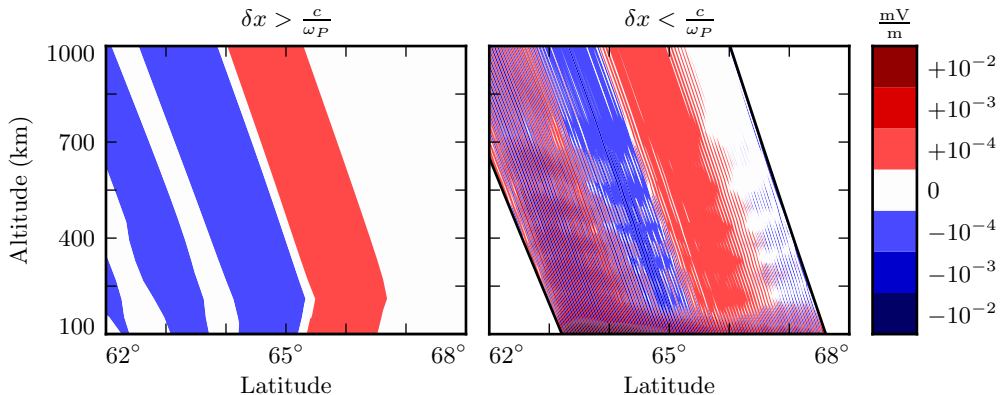


Figure 6.5: The parallel electric field develops significant structure when the perpendicular grid resolution is smaller than the electron inertial length. Unfortunately, such runs are prohibitively expensive. The lower panel — which still fails to resolve wave structure properly — represents a 100-fold increase in computational time.

Even so, the run presents a significant computational expense. Spread over 16 cores, a 100s run on Tuna’s usual grid takes well under an hour. The inertial-scale run barely finished in 96 hours, the cutoff at the Minnesota Supercomputing Institute⁶.

⁶Runtime goes as the inverse square of grid resolution. Not only does finer resolution require more grid cells, but it also gives rise to proportionally smaller crossing times, imposing a smaller time step.

The snapshot shown in Figure 6.5 uses a perpendicular grid resolution of 0.7 km at the Earthward edge, which just satisfies the Nyquist rate for the minimum inertial length of 1.7 km. It’s still too coarse. There is clearly some small-scale structure developing in the ionosphere, but it’s not well resolved. The large number of “wiggles” portends an imminent crash.

Electron inertial effects present a promising first-principles-based approach to investigate parallel currents and electric fields associated with field line resonances. Unfortunately, because of the large differences in scale between Pc4 pulsations and the plasma oscillation, the proper deployment of inertial effects presents a prohibitive computational expense. For this reason, results presented in Chapter 7 make use of the core version of Tuna presented in Chapter 5, which does not include the effects of electron inertia.

Chapter 7

Numerical Results

TODO: This chapter is the real moneymaker. The overarching motivation for this work is that $Pc4$ pulsations vary in interesting ways with respect to azimuthal modenumber, and that prior models have been unable to give a good picture of that behavior.

7.1 Finite Poloidal Lifetimes

In his 1974 paper, Radoski argues that a poloidally-polarized wave should asymptotically rotate to the toroidal polarization[80] as a result of the curved derivative in the meridional plane. The question of finite poloidal lifetimes is considered further in a 1995 paper by Mann and Wright[65]. Their numerical work used a straightened field line, with an Alfvén speed gradient in the “radial” direction. They also found a rotation over time from poloidal to toroidal polarization, with the characteristic time proportional to the azimuthal modenumber.

TODO: Ding et al[21] did similar work just before Mann and Wright, but results were less clear, possibly due to issues with grid resolution (as discussed in [65]).

TODO: Mann and Wright looked specifically at second harmonics. This work is on first harmonics. (In principle Tuna allows arbitrary driving waveforms and spatial distributions.)

The present section builds on the aforementioned results by relaxing several of their nonphysical assumptions. First, Tuna’s geometry (as described in Chapter 5) is far more realistic than Radoski’s half-cylinder or the box model used by Mann and Wright. Magnetic field lines are dipolar. Alfvén speed is based on an empirical profile, and varies along and across field lines. Next, the present results feature driving delivered over time through perturbation of the ring current; past work has instead considered the evolution of an initial condition. Finally, the present model includes a height-resolved ionosphere (rather than perfectly-reflecting boundaries). The ionospheric conductivity provides a direct coupling between the poloidal and toroidal modes, in addition to dissipating energy.

Each subplot in Figures 7.1 to 7.3 is analogous to Mann’s Figure 3. Blue lines show the total energy in the poloidal mode as a function of time. Red lines show toroidal energy. Runs are organized such that driving frequency is constant down each column, and azimuthal modenumber is constant across each row. Axis bounds are held constant across all subplots.

Energy is computed per Poynting’s theorem, with due consideration of the unusual geometry. Energy density is integrated over the meridional plane, but not in the azimuthal direction, giving units of gigajoules per radian; more than anything else, this serves as a reminder that the waves under consideration are azimuthally localized.

$$U_P = \int \frac{du^1 du^3}{2\mu_0 \sqrt{g}} \left(B_x^2 + \frac{1}{v_A^2} E_y^2 \right) \quad U_T = \int \frac{du^1 du^3}{2\mu_0 \sqrt{g}} \left(B_y^2 + \frac{1}{v_A^2} E_x^2 \right) \quad (7.1)$$

The twenty-eight runs shown in Figure 7.1 use a high-conductivity profile, corresponding to the dayside with high solar activity.

The fact that red (toroidal) lines appear at all speaks to the coupling of the poloidal and toroidal modes. As discussed in Chapter 5, driving in Tuna is delivered purely into the poloidal electric field (as a proxy for the azimuthal current).

As predicted, the rotation from poloidal to toroidal is slowest at large azimuthal mode-numbers. The toroidal energy overtakes the poloidal energy within a single drive period at $m = 4$; with $m = 64$, the most of the energy is in the poloidal mode for ~ 10 periods.

Poloidal (Blue) and Toroidal (Red) Energy: Quiet Day

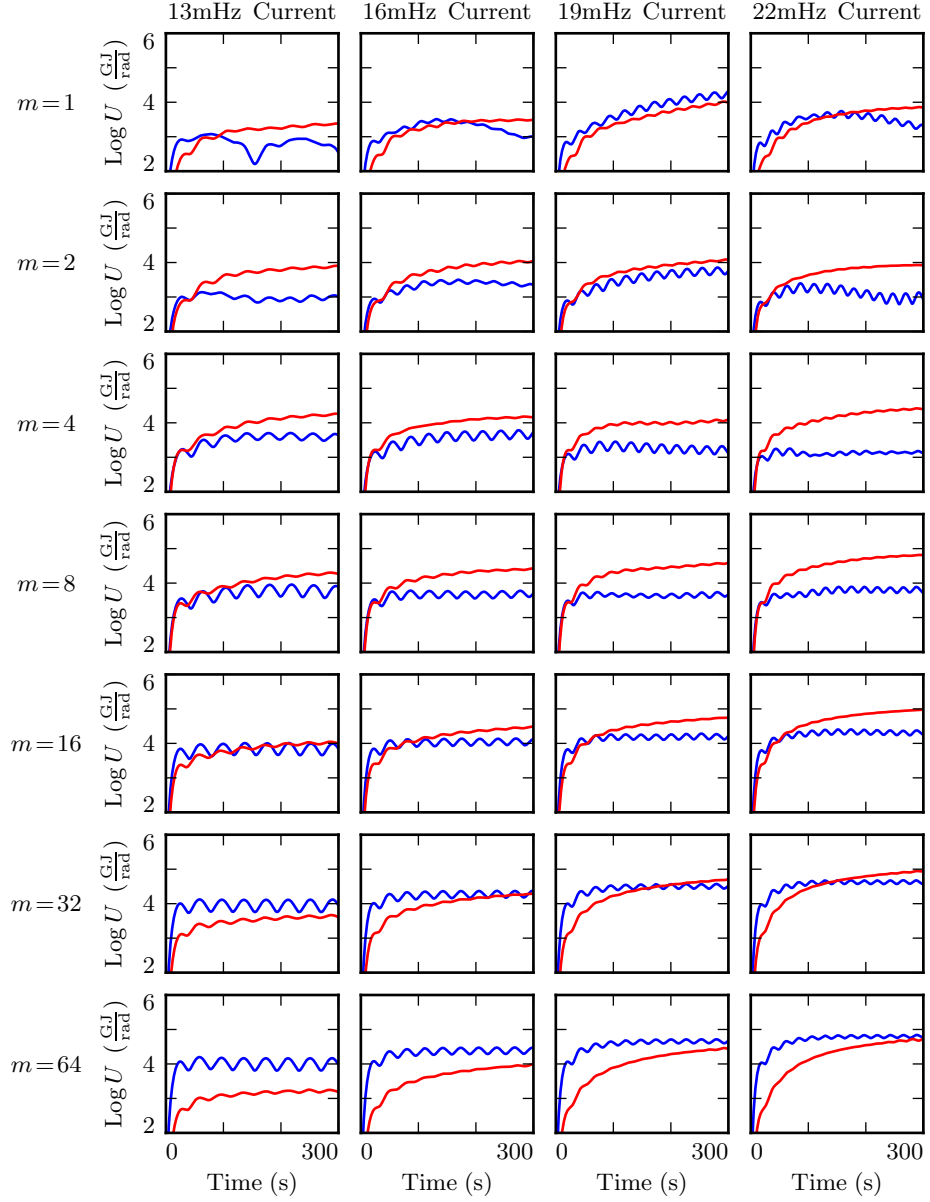


Figure 7.1: TODO: MAKE THIS PLOT WITH MODEL 2.

However, the relationship between azimuthal modenumber and rotation timescale is not linear, as was suggested by Mann and Wright. Instead, the rotation is fastest at $m = 4$.

This hints at two competing effects, and there are only so many options. In addition to the poloidal-to-toroidal rotation, the two modes are coupled by the ionospheric Hall conductivity; energy is also lost when waves propagate out of the simulation domain, and as a result of Joule dissipation.

TODO: The propagation of energy out of the simulation domain does explain this behavior. As shown in Figure 4.1, as the azimuthal modenumber increases past order unity, the cutoff frequency for compressional Alfvén waves rises through the Pc4 frequency band.

TODO: In practice, the Hall conductivity does not move large amounts of energy between the poloidal and toroidal modes. In fact, when the runs shown in Figure 7.1 are repeated with the Hall conductivity uniformly zero, the behavior is the same.

TODO: Joule dissipation is a major player in the simulation's energy economy. The asymptotic total energy is set by the balance of driving input and dissipative loss. However, it's not obvious that Joule dissipation should act particularly strongly at small azimuthal modenumber.

TODO: The total energy in the system is asymptotically determined by the balance between the energy input (from driving) and the energy loss (through Joule dissipation in the ionosphere). When the driving frequency is not particularly close to the local Alfvén frequency, the energy reaches its asymptotic value quickly. When those frequencies align closely, energy accumulates over a larger number of drive periods, and the asymptotic value is larger.

The system's resonant frequency (for a fundamental poloidal mode at $L = 5$) is affected significantly by the size of the plasmasphere. In Figure 7.1, with the plasmapause at $L_{PP} = 4$, the system resonates at 19 mHz at low m ; as m becomes large, the resonant frequency is closer to 22 mHz. Figure 7.2 shows the effect of moving the plasmapause to $L_{PP} = 5$: resonance is closer to 16 mHz. The runs are otherwise identical to those shown in Figure 7.1.

On the nightside, the picture changes significantly.

Poloidal (Blue) and Toroidal (Red) Energy: Quiet Day , $L_{PP} = 5$

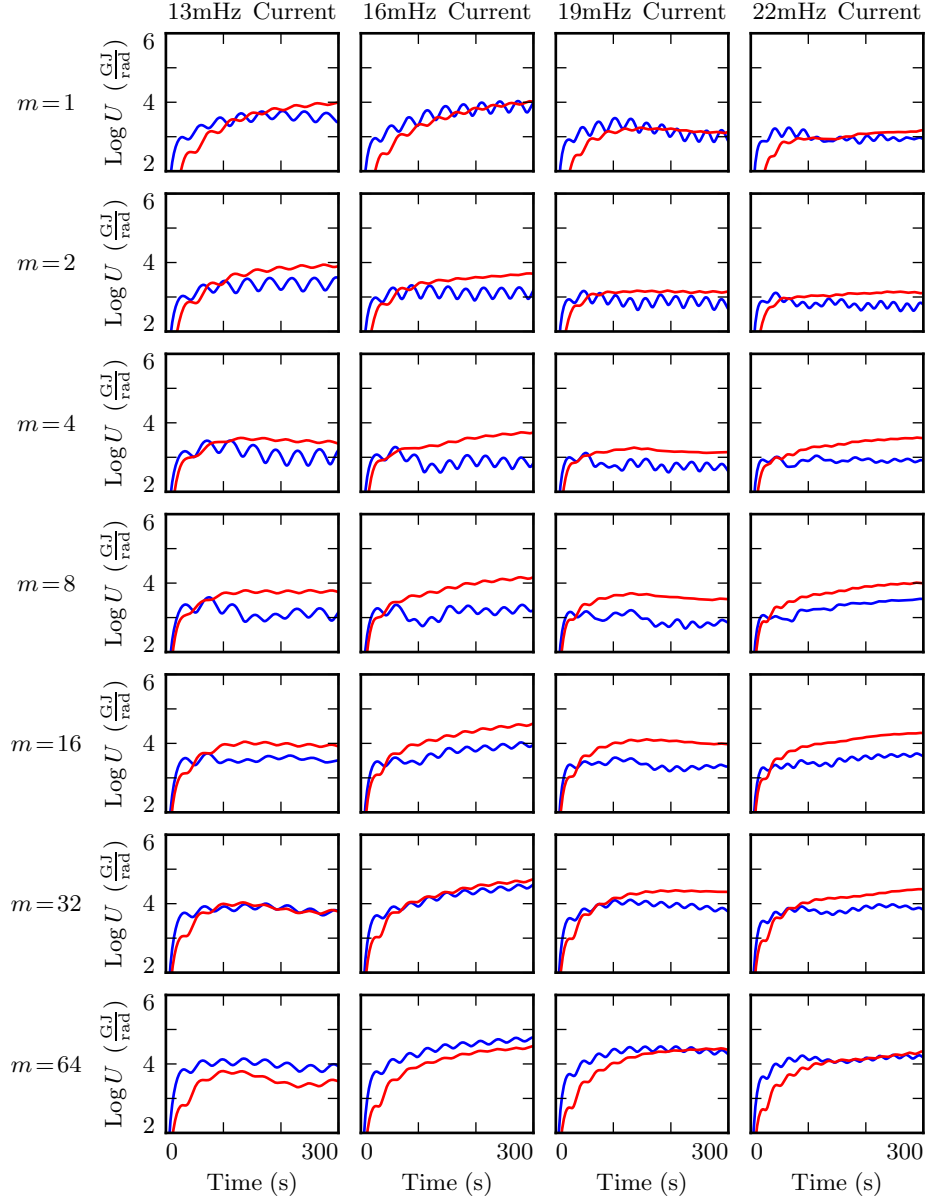


Figure 7.2: Changing the position of the plasmapause has a significant effect on the Alfvén bounce time. **TODO: FIX PLOT TITLE.**

The ionospheric conductivity on the nightside is lower. As a result, energy is dissipated more efficiently.

TODO: The asymptotic energy — at which driving and dissipation balance — is much lower on the nightside. It's reached much more quickly as a result. The system does not accumulate energy over multiple driving periods.

TODO: The system resembles a damped-driven oscillator. There is no evidence of resonance — of an energy buildup over multiple driving periods. Instead, the energy follows the waveform of the driver.

TODO: The only difference between the runs shown in Figure 7.1 and those in Figure 7.3 is the ionospheric profile.

TODO: Rotation of poloidal energy to the toroidal mode is present on the nightside, as it is on the dayside. There's less energy, of course, because the ionosphere damps the poloidal mode just as fast as it can rotate. The toroidal mode also doesn't last long.

TODO: The rotation rate is shown by the asymptotic division of energy between the poloidal and toroidal modes. As on the dayside, the toroidal mode grows most quickly at $m = 4$; the poloidal and toroidal modes hold a similar amount of energy. At $m = 64$, the dissipation timescale is evidently much faster than the rotation timescale... only $\sim 1\%$ of the poloidal energy ever rotates to the toroidal mode.

The results of the present section show agreement with — and significant refinement of — earlier work. In the case of large-but-finite ionospheric conductivity, dipole geometry, and realistic Alfvén speed profile, energy rotates asymptotically from the poloidal mode to the toroidal mode. The rotation rate is strongly affected by azimuthal modenumber and, in the case of large-but-finite m , has a characteristic timescale in the tens of periods.

The present work furthermore considers the issue of poloidal lifetimes in the low conductivity regime (while past work has used perfectly-reflecting boundaries). The result is novel: rather than asymptotically accumulating energy in the toroidal mode, an FLR on the nightside does not seem to accumulate energy at all. This is relevant to the question of day-night asymmetry in the observation of field line resonances.

Poloidal (Blue) and Toroidal (Red) Energy: Quiet Night

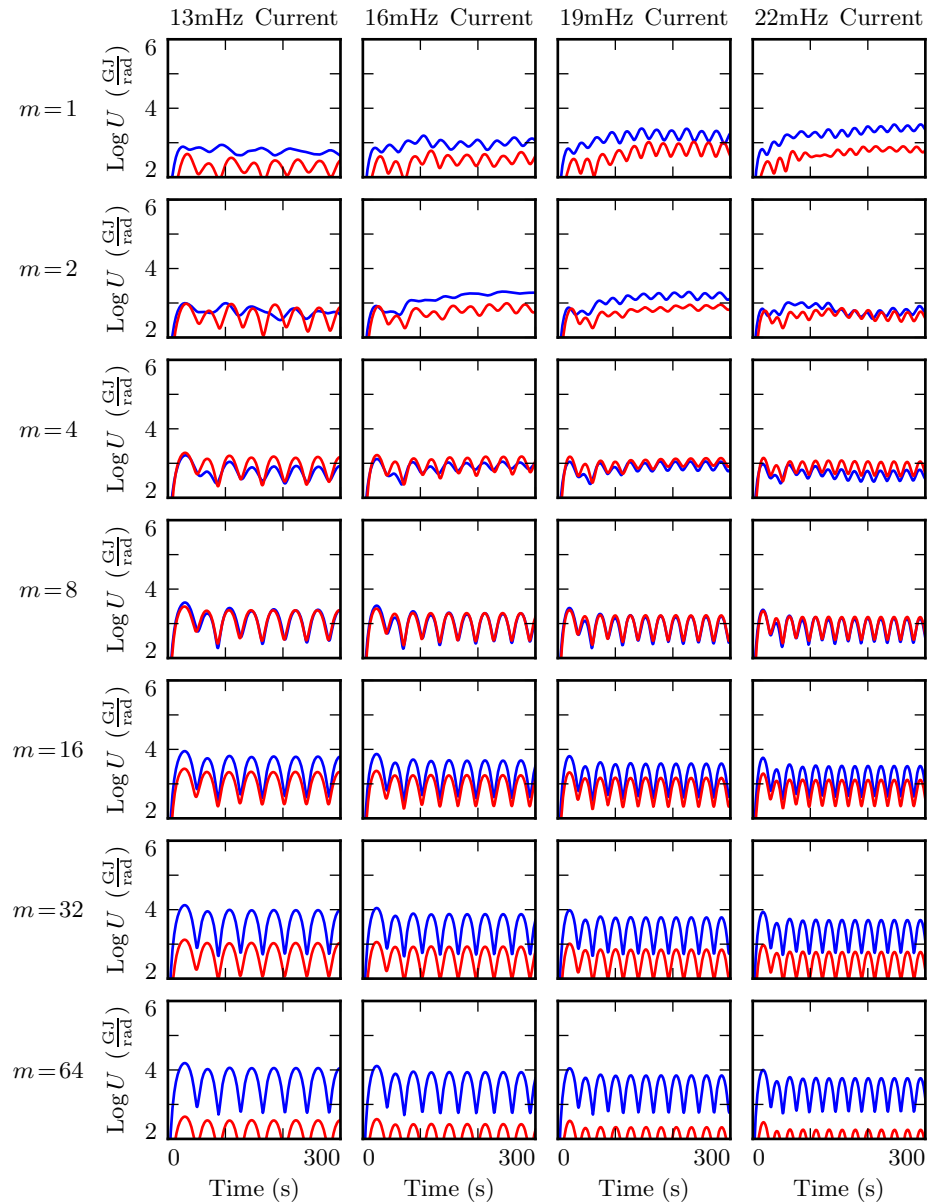


Figure 7.3: TODO: REDO WITH MODEL 2.

7.2 Spatial Distribution of Energy

Looking a bit deeper, it's possible to comment on the structure of the poloidal and toroidal modes, not just their magnitudes.

TODO: Probably should at least mention the nightside? It seems silly to leave it out.

In the following figures, energy density is computed at each grid point, then averaged over the volume of the flux tube (again, with proper respect to the unusual geometry). This allows the eyeballing of how energy moves across field lines as a function of time. The color scale is shared across all plots.

Poloidal and toroidal energy are again considered separately. The two exhibit qualitatively different behavior.

TODO: At low m , energy rotates out of the poloidal mode so quickly that no resonance can form.

TODO: At high m , the Alfvén wave is guided. If the driving frequency lines up with the resonant frequency where it's delivered, the poloidal mode resonates strongly. Otherwise, again, no energy accumulates.

TODO: In no case does the poloidal mode demonstrate the ability to move energy across magnetic field lines.

TODO: On the other hand, the toroidal mode does resonate, even if the driving isn't resonant (though in that case the response is of course stronger). The toroidal mode transports energy across field lines until it encounters resonance, then accumulates energy there. Often, resonances are seen in multiple locations due to the non-monotonic Alfvén bounce frequency as a function of L .

TODO: The stuff at the top is the 3rd harmonic.

TODO: If m is small, energy rotates to the toroidal mode too fast to form a poloidal resonance. If m is large, the Alfvén wave is guided, so it resonates only if the driving frequency lines up with the resonant frequency where it's applied. The result is just one big — or perhaps even giant — pulsation. If the driving lines up with a nearby field line, the toroidal mode goes crazy! Resonance inside the plasmasphere. Resonance at

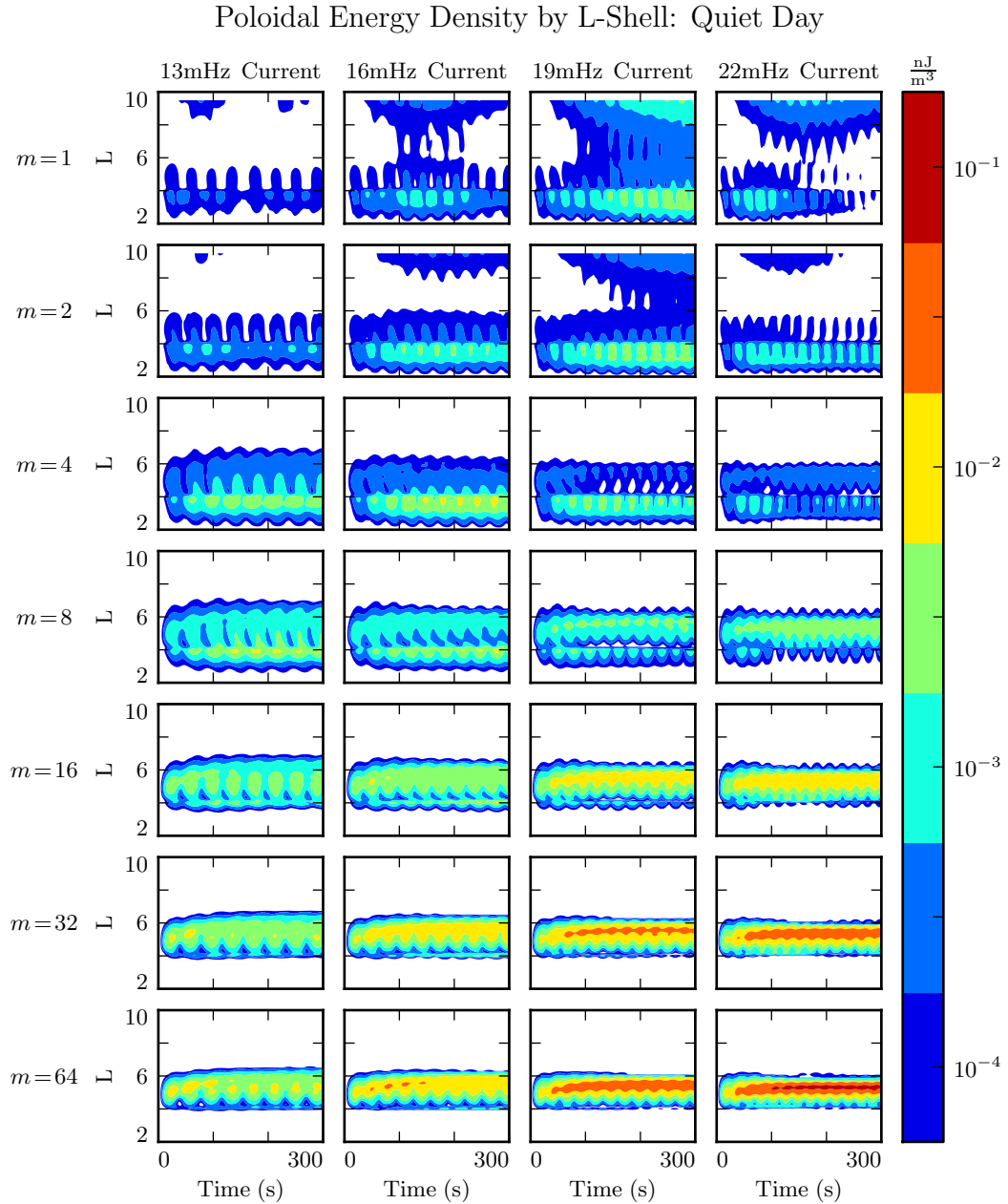


Figure 7.4: TODO: ...

the plasmapause. Resonance at the driving location. And (weak) attempt at a higher harmonic further out.

TODO: When the driving frequency doesn't line up with the location where it's delivered, there's basically no response. There is no movement of energy to a resonant field line, so no energy can accumulate over the course of multiple rounds of driving. Even when not driven resonantly, the toroidal mode still makes the best of its situation. It steals what energy it can from the poloidal mode, carries it to the resonant L -shell, and gets to work. (In contrast, recall from ??, in this situation the poloidal mode just does not accumulate energy.)

TODO: Why is this exciting?

TODO: Driving from inside the magnetosphere is novel.

TODO: Why is this exciting?

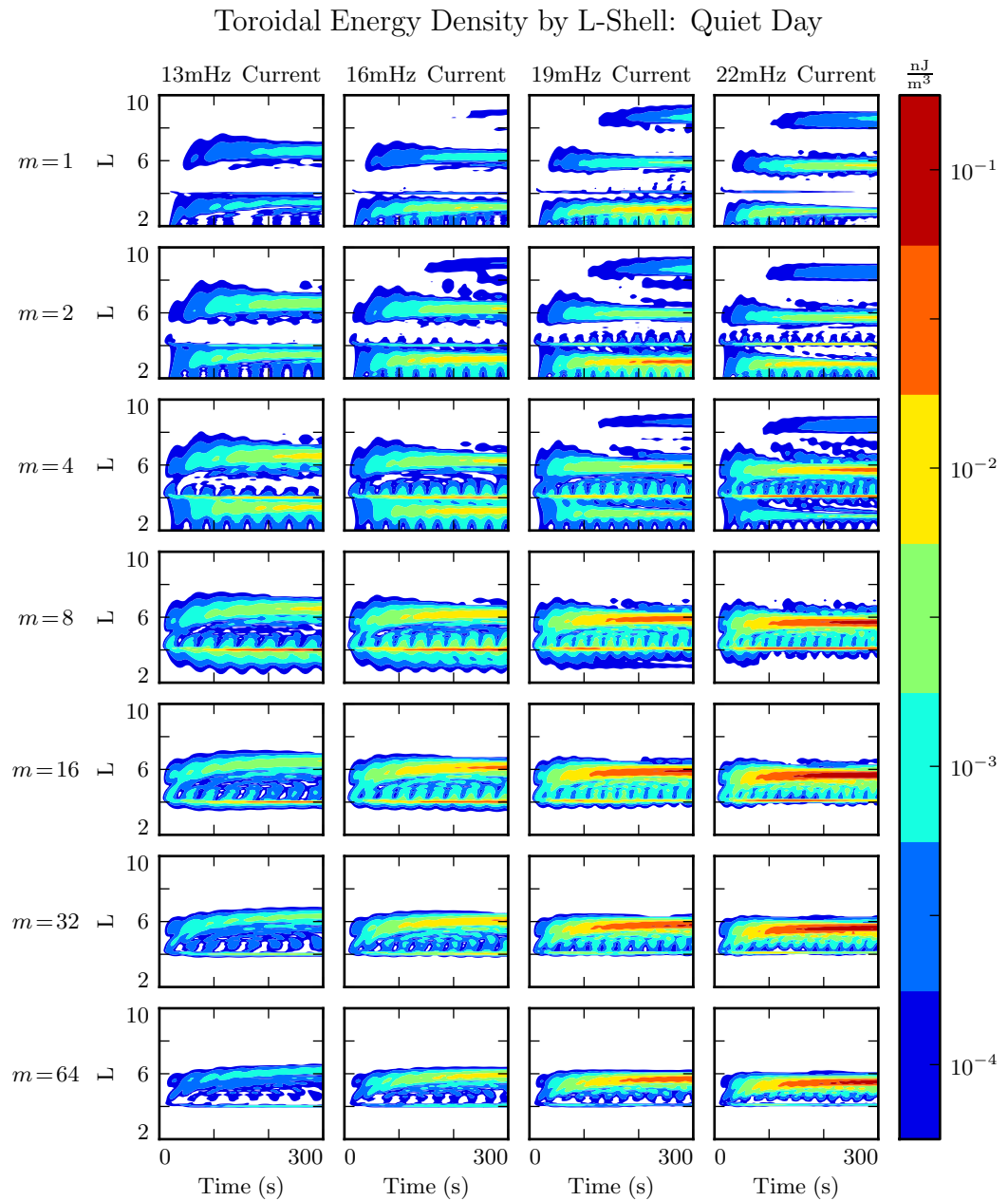


Figure 7.5: TODO: ...

7.3 Significance for Giant Pulsations

Giant pulsations are (probably[91]) fundamental mode poloidal $Pc4$ pulsations with frequencies around 10 mHz and azimuthal modenumber around 20. They are large, and can sometimes be observed on the ground.

While this model makes no particular distinction between a giant pulsation and any other $Pc4$, the above results do line up with giant pulsation observations.

Giant pulsations aren't seen at small m . As shown in Section 7.1, low- m poloidal modes rotate to the toroidal mode too quickly to resonate effectively, even in the case of continuous driving at a locally-resonant frequency. The sweet spot seems to be around $m = 20$, more or less the same point where resonance becomes visible in ???. Admittedly, giant pulsations are typically closer to 10 mHz than 22 mHz. It seems likely that qualitatively similar results would be encountered if the driving were moved to an L -shell with a bounce time of 10 mHz.

TODO: Present profiles do not allow a distinction between the dawn and dusk flank.
Future work... Tuna could easily accept new profiles!

TODO: [91] talks significantly about the east-west polarization.

Giant pulsations are seen at very large m , though not on the ground[92], due to damping by the ionosphere.

Giant pulsations are most common on the dayside (particularly the morningside), during geomagnetically quiet times. Giant pulsation ground signatures are noted for their predisposition towards east-west polarization.

In Figure 7.6, the strongest east-west ground signatures is obtained on the geomagnetically quiet dayside, at m of 16 and 32.

This seems to be a giant pulsation "sweet spot": the poloidal mode becomes stronger as m increases, but the ionospheric damping also increases.

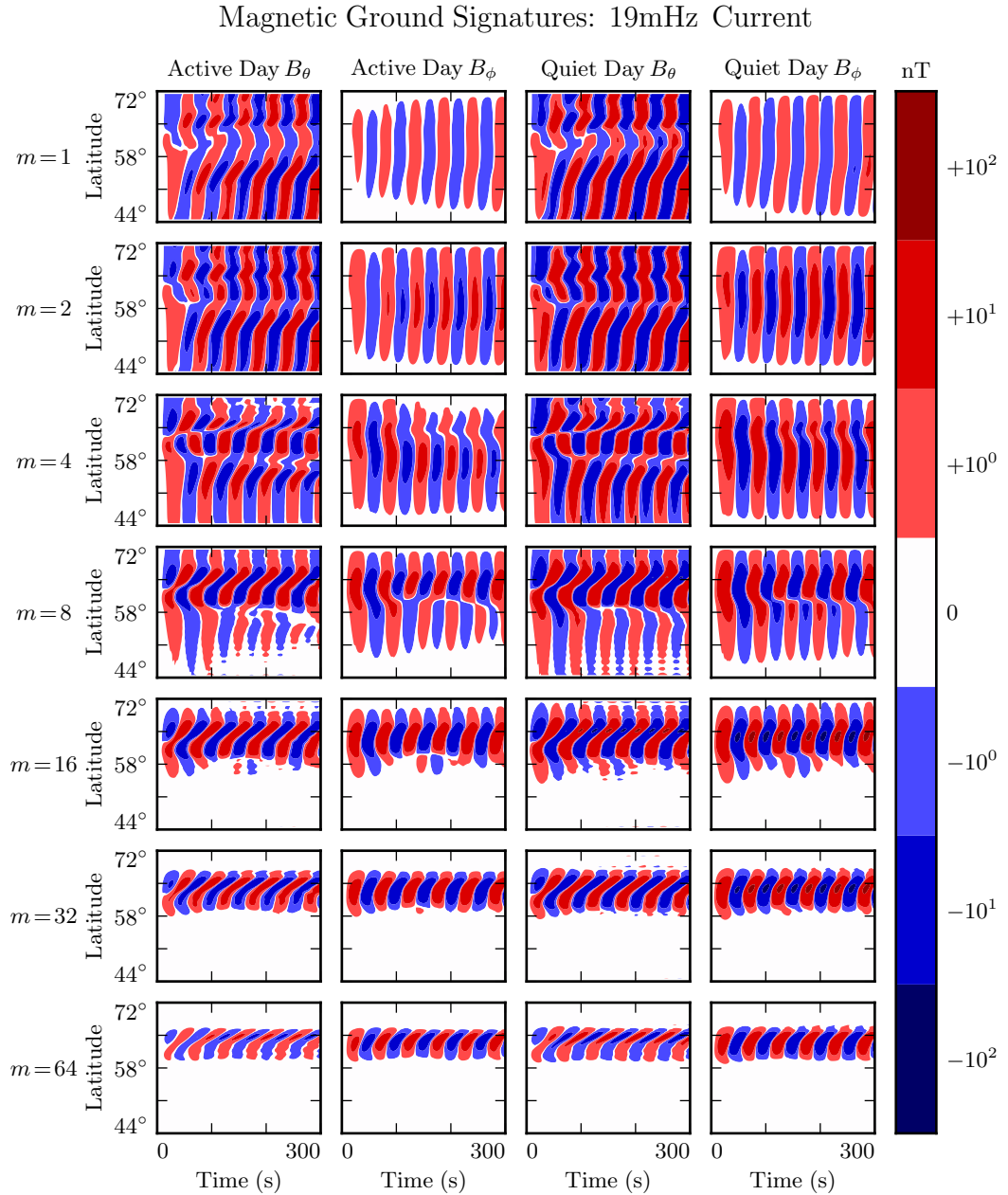


Figure 7.6: The east-west component of magnetic ground signatures is peaked on the geomagnetically quiet dayside, at modenumbers around 16 to 32. This coincides nicely with observations of giant pulsations. Like the east-west component, the north-south ground signature is strongest on the quiet dayside; however, unlike the east-west component, the north-south component is weak when the modenumber is large.

Giant pulsations are monochromatic, and can be accompanied by “multiharmonic toroidal waves”[91]. Per Section 7.2, this is about what would be expected from a mishmash of poloidal driving. Poloidal modes of all frequencies rotate into the toroidal mode; resonant poloidal modes resonate; non-resonant poloidal modes become evanescent.

Giant pulsations often drift azimuthally. This model can’t resolve azimuthal drift directly, of course, but can fake it by looking at complex phase. There has been some indication (not shown) of complex phase rotation in ground magnetic fields. However, at the boundary, it’s difficult to disentangle which values are imaginary to indicate an azimuthal offset, and which are imaginary because of Hall coupling. Investigation is ongoing.

Chapter 8

Observations

TODO: You know what would be great for putting this numerical work in context? A nice, consistent survey that breaks down the occurrence rate of Pc4 pulsations by harmonic, etc.

TODO: There have been some surveys in the past. Dai did a nice one last year, but his filter biased him against the fundamental mode. And only a few past works have even worried about harmonic mode... probably because it's hard to get that information unless you have both E and B.

TODO: Furthermore, it's awkward that Pgs are identified by visual inspection. How can we say how rare they are if they aren't rigorously defined?

8.1 Event Selection

TODO: Scroll through the entire almost-three-year duration of the Van Allen Probes mission so far. Both probes.

TODO: Spinfit the field measurements to clean them up. This gives a ten-second cadence. Events are half an hour long to ensure that there are enough points to get a decent DFT.

TODO: Also take $\underline{E} \cdot \underline{B} = 0$ to clean up the electric field. Notably, Dai did not do this (since he did not need the electric field). Any data within 15° of the probe's spin axis is discarded as part of this process. This is a significant portion of the data — about half — and furthermore introduces a bias in MLT, as discussed in Section 8.2. Map the field to GSE coordinates to be consistent with the probe's position.

TODO: Take a ten-minute rolling average of the data to get the background magnetic field. Subtract it out, and set $\hat{z} \parallel \underline{B}_0$. Then get the azimuthal direction with $\hat{y} \parallel \underline{B}_0 \times \underline{r}$. The third component is the crosswise direction, $\hat{x} \equiv \hat{y} \times \hat{z}$. This is the same technique described by Liu[57].

TODO: Compute discrete Fourier transforms: $\tilde{\underline{E}}_x$, $\tilde{\underline{E}}_y$, $\tilde{\underline{B}}_x^*$, $\tilde{\underline{B}}_y^*$. Then get the poloidal and toroidal Poynting flux, mapped to the ionosphere (giving a factor of L^3 for the compression of the flux tube).

$$\tilde{S}_P \equiv -\frac{L^3}{\mu_0} \tilde{E}_y \tilde{B}_x^* \quad \tilde{S}_T \equiv \frac{L^3}{\mu_0} \tilde{E}_x \tilde{B}_y^* \quad (8.1)$$

TODO: Find the largest IMAGINARY component of the Poynting flux. This is the biggest standing wave present in this half hour.

TODO: Threshold on frequency: anything not in the Pc4 frequency range gets tossed.

TODO: Threshold on magnitude: anything below 10^{-2} mW/m^2 gets tossed.

TODO: Threshold on coherence: if $\tilde{\underline{E}}$ and $\tilde{\underline{B}}^*$ aren't coherent at 0.9 or better, the event gets tossed. .

TODO: Notably, there is NO threshold on spectral width. Broadband and messy signals are allowed. See Figure 8.2.

TODO: We try not to worry too much about first vs third harmonic, since we can't tell them apart except by guessing at frequency. Chisham and Orr[14] argue that around $7 R_E$, frequency around 10 mHz precludes higher harmonics. Or maybe look at [35]?

8.2 Bias in MLT

TODO: RBSP precesses over time. It took about 22 months to go all the way around Earth. In principle, this gets rid of any bias in MLT. However, because the spin plane faces the sun, we lose more data to $\underline{E} \cdot \underline{B} = 0$ on the flanks.

TODO: It's not worth trying to get uniform coverage, then. We instead go for all available data. Almost 3 years of data from each probe.

TODO: This comes out to ... probe-days between $L = 4$ and $L = 6$. Comparable to about a year from a ground magnetometer?

TODO: The plots in section ... are normalized by Figure 8.1. This is as close as we can get to cutting out the bias.

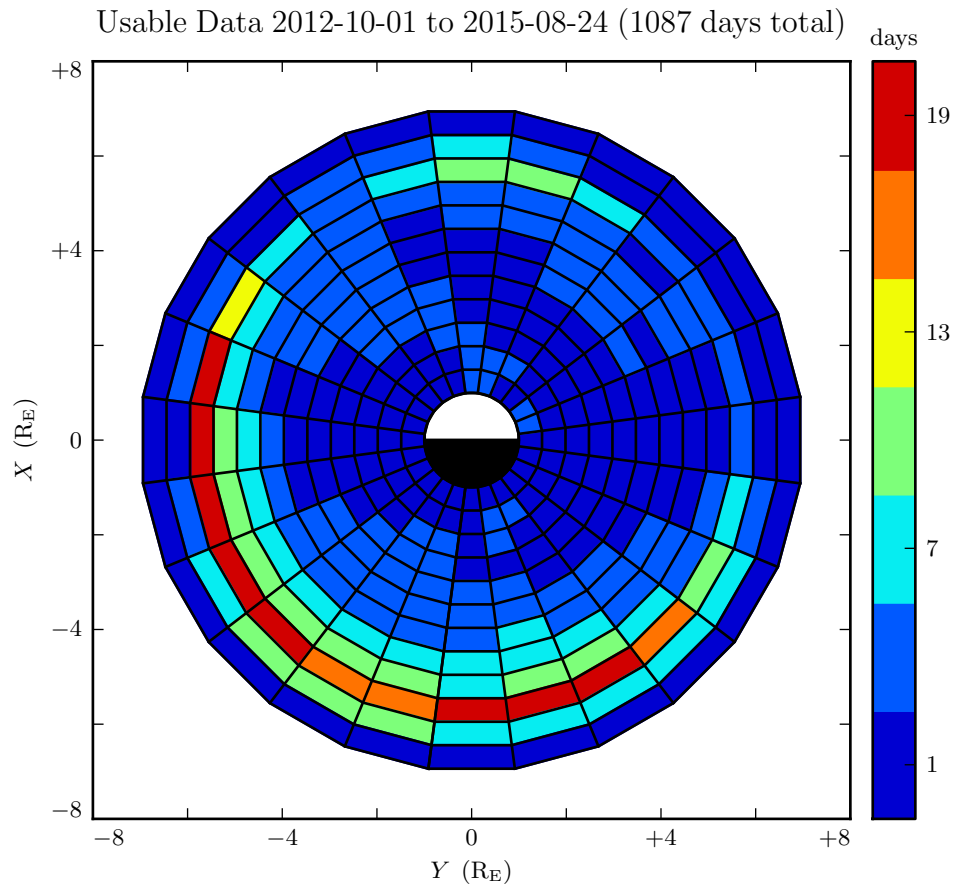


Figure 8.1: Electric field data is cleaned up by taking $\underline{E} \cdot \underline{B} = 0$. If the field is within 15° of the spin axis, that assumption is not reliable, so the data is discarded. Doing so biases the sample against the flanks. (The concentration near $L = 6$ is due to the probes' slower movement near apogee.)

8.3 Slicing Events One Way...

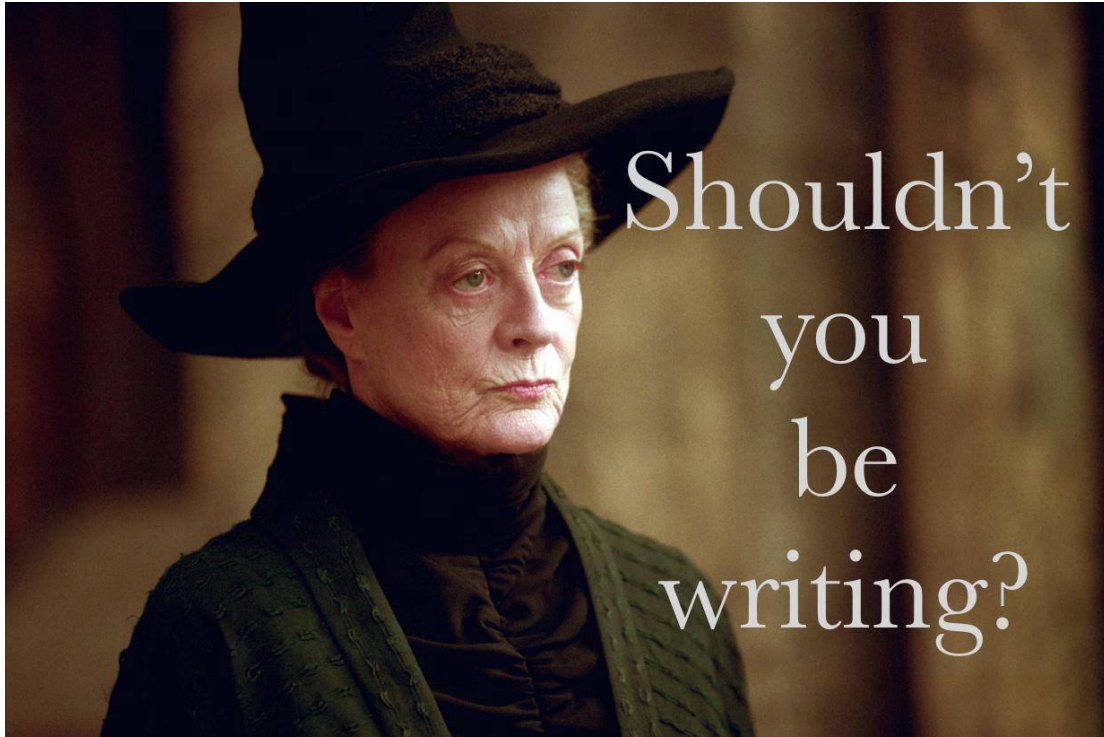


Figure 8.2: TODO: Break into three bins by FWHM.

8.4 Slicing Events Another Way...

TODO: Of the \sim 100 events where both the poloidal and toroidal channels triggered independently, almost all had one odd mode and one even mode.

TODO: Collections of events at a single ground observatory (near 66°) over significant periods of time:

Brekke[7] looked at 523 giant pulsation events recorded at Tromsø, Norway, from 1929 to 1985. This spanned several solar cycles.

Rolf[82] collected 28 events between 1921 and 1930 at Abisko.

Sucksdorf[89] got 150 events between 1914 and 1938 in Sodankylä.

Harang[40]. 97 events from 1929 to 1941. Also Tromsø. Note that this may have been limited by the war!

This comes out to something like ... events over ... years. That's about ... giant pulsations per year, observed on the ground.

TODO: Collections of events at an array of ground observatories:

Chisham and Orr[14] found 34 events from 1984 to 1987 using the EISCAT magnetometer array in Scandinavia. About 5° in MLT, decent coverage from 63° to 67° mlat. This coincides with a solar minimum.

Motoba, in 2015, recorded 105 giant pulsation events. The observations were carried out by a number of ground magnetometers spanning $\sim 90^\circ$ in local time and ranging roughly 60° to 70° magnetic latitude[71]. This was mostly during a period of low solar activity, so we expect a high count.

TODO: Estimate of the size of an event's footprint:

Velkamp[100] looked at a single large event and showed that, at best, it was visible over a span of 5° in magnetic latitude.

This is seemingly consistent with the 29 February 2012 event discussed in detail by Motoba[71] — Motoba shows some data, but doesn't discuss this aspect in detail.

Takahashi[91] computes a FWHM of about 1 in L, or 2° magnetic latitude.

TODO: Tying that in to RBSP observations?

Note that it's a bit tricky to compare ground observations to in situ observations. Large- m events won't make it through the ionosphere.

There should be no bias with respect to MLT between a ground magnetometer and RBSP. Dai's analysis was specifically chosen to take advantage of the fact that RBSP's orbit had precessed all the way around the Earth. No preferred direction. And mlat shouldn't cause issues... these are FLRs, after all.

How strong does an event need to be on the ground, or in the sky, to count as a giant pulsation? Motoba 2015[71] has an event which tops out on the order of 10 nT on the ground. It's more like 5 mV/m in situ. Takahashi[91] has similar values.

Note that Takahashi[92] has shown that it's OK to call something a giant pulsation even if it's not visible on the ground... though, obviously, we are comparing to ground magnetometer data for occurrence rate.

If peak Pg observations are at 66° mlat, that corresponds to $L = 6$. Then let's suppose that peak Pg viewing is 5° wide — estimating from the work of Velkamp and Motoba. That means RBSP should see lots of Pgs when it's between $L = 5.2$ and $L = 7.1$. Well, $7.1 R_E$ is outside its apogee, but the probes spend a fair amount of time outside $L = 5.2$, since they are moving pretty slowly at that point.

Giant pulsations have been shown to be more numerous in times of low solar activity. That was the whole point of Brekke's seminal 1987 paper, and it's consistent with what we show in Section 7.3. The RBSP observations occur during peak solar times, though it's an anemic solar peak[76].

TODO: How much time does RBSP spend outside of $L = 5.2$ (for a range of 5°)? How about $L = 5.6$ to $L = 6.5$ (for FWHM of 2°)?

Each RBSP probe spends about 30 % of its orbit between $L = 5.6$ and $L = 6.5$.

RBSP-A and RBSP-B count as two observers. In one ~ 5 cases out of hundreds do they simultaneously observe a poloidal Pc4 event (although, most notably for the 2012 event which [18] considers in detail), both probes do fly through the same apparent event several hours apart from one another.

The duration of Dai's survey is October 2012 to June 2014. Scaled by 2 probes, each of which is present in the peak Pg lshells 30% of the time, that comes out to almost exactly one year.

TODO: How many fundamental mode poloidal events do we see? How many could pass for giant pulsations? How many should we expect to see?

TODO: How weird is it for a fundamental mode poloidal Pc4 to be monochromatic?

TODO: How weird is it for a fundamental mode poloidal Pc4 to be stronger than 5 mV/m at the equator?

Chapter 9

Conclusion

9.1 Summary of Results

TODO: Code development.

TODO: Numerical results.

TODO: Observational results.

9.2 Future Work

TODO: Code development.

Arbitrary deformation of grid. Get $\hat{e}_i = \frac{\partial}{\partial u^i} \underline{x}$, then $g_{ij} = \hat{e}_i \cdot \hat{e}_j$, then invert the metric tensor for contravariant components.

MPI. Some benchmarks with time to compute vs time to broadcast. This might make sense for inertial length scales.

Better ionospheric profiles. Distinction between the dawn and dusk flanks. Maybe even update the conductivity based on energy deposition — precipitation causes ionization!

IRI ionosphere model. Solar illumination effects.

TODO: Numerical work.

More complicated driving. Higher harmonics, non-sinusoidal waveforms. Maybe even drive based on events/Dst?

Look at runs with a plasmasphere further out. Can we get nicer resonance on the nightside? A larger plasmapause will cause L=5 to line up better with Pc4 frequencies.

TODO: Data analysis.

Look at distribution of these events with respect to the plasmapause, storm phase...

References

- [1] S.-I. Akasofu. The development of the auroral substorm. *Planetary and Space Science*, 12(4):273–282, 1964.
- [2] H. Alfvén. On the cosmogony of the solar system III. *Stockholms Observatoriums Annaler*, 14:9.1–9.29, 1946.
- [3] B. J. Anderson, M. J. Engebretson, S. P. Rounds, L. J. Zanetti, and T. A. Potemra. A statistical study of Pc 3-5 pulsations observed by the AMPTE/CCE magnetic fields experiment, 1. occurrence distributions. *J. Geophys. Res.*, 95(A7):10495, 1990.
- [4] V. Angelopoulos. The THEMIS mission. *Space Science Reviews*, 141(1-4):5–34, 2008.
- [5] K. Birkeland. Expédition norvégienne de 1899-1900 pour l'étude des aurores boréales. *Mat. Naturvidensk. Kl.*, KI(I), 1901.
- [6] J. P. Boris. A physically motivated solution of the Alfvén problem. *NRL Memorandum Report*, 2167, 1970.
- [7] A. Brekke, T. Feder, and S. Berger. Pc4 giant pulsations recorded in Tromsø, 1929-1985. *Journal of Atmospheric and Terrestrial Physics*, 49(10):1027–1032, 1987.
- [8] C. W. Carlson, R. F. Pfaff, and J. G. Watzin. The fast auroral Snapshot (FAST) mission. *Geophys. Res. Lett.*, 25(12):2013–2016, 1998.

- [9] A. A. Chan, M. Xia, and L. Chen. Anisotropic alfvén-balloonning modes in Earth's magnetosphere. *J. Geophys. Res. Space Physics*, 99(A9):17351–17366, 1994.
- [10] L. Chen and A. Hasegawa. A theory of long-period magnetic pulsations: 1. steady state excitation of field line resonance. *J. Geophys. Res.*, 79(7):1024–1032, 1974.
- [11] L. Chen and A. Hasegawa. Kinetic theory of geomagnetic pulsations: 1. internal excitations by energetic particles. *J. Geophys. Res.*, 96(A2):1503, 1991.
- [12] L. Chen, R. White, C. Cheng, F. Romanelli, J. Weiland, R. Hay, J. V. Dam, D. Barnes, M. Rosenbluth, and S. Tsai. Theory and simulation of fishbone-type instabilities in beam-heated tokamaks. Technical report, 1984.
- [13] C. Z. Cheng and Q. Qian. Theory of ballooning-mirror instabilities for anisotropic pressure plasmas in the magnetosphere. *J. Geophys. Res.*, 99(A6):11193, 1994.
- [14] G. Chisham and D. Orr. Statistical studies of giant pulsations (pgs): Harmonic mode. *Planetary and Space Science*, 39(7):999–1006, 1991.
- [15] W. D. Cummings, R. J. O'Sullivan, and P. J. Coleman. Standing Alfvén waves in the magnetosphere. *J. Geophys. Res.*, 74(3):778–793, 1969.
- [16] L. Dai. Collisionless magnetic reconnection via Alfvén eigenmodes. *Phys. Rev. Lett.*, 102(24), 2009.
- [17] L. Dai, K. Takahashi, R. Lysak, C. Wang, J. R. Wygant, C. Kletzing, J. Bonnell, C. A. Cattell, C. W. Smith, R. J. MacDowall, S. Thaller, A. Breneman, X. Tang, X. Tao, and L. Chen. Storm time occurrence and spatial distribution of Pc4 poloidal ULF waves in the inner magnetosphere: A Van Allen Probes statistical study. *J. Geophys. Res. Space Physics*, 120:4748–4762, 2015.
- [18] L. Dai, K. Takahashi, J. R. Wygant, L. Chen, J. Bonnell, C. A. Cattell, S. Thaller, C. Kletzing, C. W. Smith, R. J. MacDowall, D. N. Baker, J. B. Blake, J. Fennell, S. Claudepierre, H. O. Funsten, G. D. Reeves, and H. E. Spence. Excitation of poloidal standing Alfvén waves through drift resonance wave-particle interaction. *Geophys. Res. Lett.*, 40:4127–4132, 2013.

- [19] A. W. Degeling, R. Rankin, and Q.-G. Zong. Modeling radiation belt electron acceleration by ULF fast mode waves, launched by solar wind dynamic pressure fluctuations. *J. Geophys. Res. Space Physics*, 119(11):8916–8928, 2014.
- [20] W. D. D’haeseleer, W. N. G. H. J. D. Callen, and J. L. Shohet. *Flux Coordinates and Magnetic Field Structure*. Springer-Verlag, New York, 1991.
- [21] D. Q. Ding, R. E. Denton, M. K. Hudson, and R. L. Lysak. An MHD simulation study of the poloidal mode field line resonance in the Earth’s dipole magnetosphere. *J. Geophys. Res.*, 100:63–77, 1995.
- [22] J. W. Dungey. The attenuation of Alfvén waves. *J. Geophys. Res.*, 59(3):323–328, 1954.
- [23] J. W. Dungey. Interplanetary magnetic field and the auroral zones. *Phys. Rev. Lett.*, 6(2):47–48, 1961.
- [24] A. Einstein. Die grundlage der allgemeinen relativitätstheorie. *Ann. Phys.*, 354:769–822, 1916.
- [25] S. R. Elkington, M. K. Hudson, and A. A. Chan. Acceleration of relativistic electrons via drift-resonant interaction with toroidal-mode Pc-5 ULF oscillations. *Geophys. Res. Lett.*, 26(21):3273–3276, 1999.
- [26] M. J. Engebretson, D. L. Murr, K. N. Erickson, R. J. Strangeway, D. M. Klumpar, S. A. Fuselier, L. J. Zanetti, and T. A. Potemra. The spatial extent of radial magnetic pulsation events observed in the dayside near synchronous orbit. *J. Geophys. Res.*, 97(A9):13741, 1992.
- [27] P. T. I. Eriksson, L. G. Blomberg, A. D. M. Walker, and K.-H. Glassmeier. Poloidal ULF oscillations in the dayside magnetosphere: a Cluster study. *Ann. Geophys.*, 23(7):2679–2686, 2005.
- [28] S. Fujita and T. Tamao. Duct propagation of hydromagnetic waves in the upper ionosphere, 1, electromagnetic field disturbances in high latitudes associated with localized incidence of a shear Alfvén wave. *J. Geophys. Res.*, 93(A12):14665, 1988.

- [29] K.-H. Glassmeier. Magnetometer array observations of a giant pulsation event. *J. Geophys.*, 48:127–138, 1980.
- [30] K.-H. Glassmeier. On the influence of ionospheres with non-uniform conductivity distribution on hydromagnetic waves. *J. Geophys.*, 54(2):125–137, 1984.
- [31] K.-H. Glassmeier, S. Buchert, U. Motschmann, A. Korth, and A. Pedersen. Concerning the generation of geomagnetic giant pulsations by drift-bounce resonance ring current instabilities. *Ann. Geophysicae*, 17:338–350, 1999.
- [32] K.-H. Glassmeier, D. Klimushkin, C. Othmer, and P. Mager. ULF waves at mercury: Earth, the giants, and their little brother compared. *Advances in Space Research*, 33(11):1875–1883, 2004.
- [33] C. Goertz. Kinetic alfvén waves on auroral field lines. *Planetary and Space Science*, 32(11):1387–1392, 1984.
- [34] C. K. Goertz and R. W. Boswell. Magnetosphere-ionosphere coupling. *J. Geophys. Res.*, 84(A12):7239, 1979.
- [35] C. A. Green. Giant pulsations in the plasmasphere. *Planetary and Space Science*, 33(10):1155–1168, 1985.
- [36] J. L. Green and S. Boardsen. Duration and extent of the great auroral storm of 1859. *Advances in Space Research*, 38(2):130–135, 2006.
- [37] C. Greifinger and P. S. Greifinger. Theory of hydromagnetic propagation in the ionospheric waveguide. *J. Geophys. Res.*, 73(23):7473–7490, 1968.
- [38] B. C. Hall. *Lie Groups, Lie Algebras, and Representations*. Graduate Texts in Mathematics. Springer, New York, second edition, 2015.
- [39] Y. X. Hao, Q.-G. Zong, Y. F. Wang, X.-Z. Zhou, H. Zhang, S. Y. Fu, Z. Y. Pu, H. E. Spence, J. B. Blake, J. Bonnell, J. R. Wygant, and C. A. Kletzing. Interactions of energetic electrons with ULF waves triggered by interplanetary shock: Van allen probes observations in the magnetotail. *J. Geophys. Res. Space Physics*, 119(10):8262–8273, 2014.

- [40] L. Harang. *Pulsations in the terrestrial magnetic records at high latitude stations*. Grondahl, 1942.
- [41] O. Hillebrand, J. Muench, and R. L. McPherron. Ground-satellite correlative study of a giant pulsation event. *Journal of Geophysics Zeitschrift Geophysik*, 51:129–140, 1982.
- [42] W. J. Hughes. Magnetospheric ULF waves: A tutorial with a historical perspective. In M. J. Engebretson, K. Takahashi, and M. Scholer, editors, *Solar Wind Sources of Magnetospheric Ultra-Low-Frequency Waves*, volume 81 of *Geophys. Monogr.*, pages 1–12. American Geophysical Union, Washington, DC, 1994.
- [43] W. J. Hughes and D. J. Southwood. The screening of micropulsation signals by the atmosphere and ionosphere. *J. Geophys. Res.*, 81(19):3234–3240, 1976.
- [44] W. J. Hughes, D. J. Southwood, B. Mauk, R. L. McPherron, and J. N. Barfield. Alfvén waves generated by an inverted plasma energy distribution. *Nature*, 275(5675):43–45, 1978.
- [45] J. A. Jacobs, Y. Kato, S. Matsushita, and V. A. Troitskaya. Classification of geomagnetic micropulsations. *J. Geophys. Res.*, 69(1):180–181, 1964.
- [46] T. Karlsson and G. T. Marklund. A statistical study of intense low-altitude electric fields observed by freja. *Geophys. Res. Lett.*, 23(9):1005–1008, 1996.
- [47] Y. Kato and T. Tsutomu. Hydromagnetic oscillations in a conducting medium with hall conduct-ivity under the uniform magnetic field. *Science reports of the Tohoku University. Ser. 5, Geophysics*, 7(3):147–164, 1956.
- [48] M. C. Kelley. *The Earth’s Ionosphere*. Academic Press, San Diego, second edition, 1989.
- [49] R. L. Kessel. Solar wind excitation of pc5 fluctuations in the magnetosphere and on the ground. *J. Geophys. Res.*, 113(A4), 2008.
- [50] D. Y. Klimushkin, P. N. Mager, and K.-H. Glassmeier. Toroidal and poloidal Alfvén waves with arbitrary azimuthal wavenumbers in a finite pressure plasma in the earth’s magnetosphere. *Annales Geophysicae*, 22(1):267–287, 2004.

- [51] S. Kokubun. Observations of Pc pulsations in the magnetosphere: Satellite-ground correlation. *J. Geomagn. Geoelec*, 32(Supplement2):SII17–SII39, 1980.
- [52] S. Kokubun, K. N. Erickson, T. A. Fritz, and R. L. McPherron. Local time asymmetry of Pc 4-5 pulsations and associated particle modulations at synchronous orbit. *J. Geophys. Res.*, 94(A6):6607–6625, 1989.
- [53] D.-H. Lee and K. Kim. Compressional MHD waves in the magnetosphere: A new approach. *J. Geophys. Res.*, 104(A6):12379–12385, 1999.
- [54] A. S. Leonovich and V. A. Mazur. Structure of magnetosonic eigenoscillations of an axisymmetric magnetosphere. *J. Geophys. Res.*, 105(A12):27707–27715, 2000.
- [55] W. Liu, J. B. Cao, X. Li, T. E. Sarris, Q.-G. Zong, M. Hartinger, K. Takahashi, H. Zhang, Q. Q. Shi, and V. Angelopoulos. Poloidal ULF wave observed in the plasmasphere boundary layer. *J. Geophys. Res. Space Physics*, 118(7):4298–4307, 2013.
- [56] W. Liu, T. E. Sarris, X. Li, S. R. Elkington, R. Ergun, V. Angelopoulos, J. Bonnell, and K. H. Glassmeier. Electric and magnetic field observations of Pc4 and Pc5 pulsations in the inner magnetosphere: A statistical study. *J. Geophys. Res.*, 114(A12), 2009.
- [57] W. Liu, T. E. Sarris, X. Li, R. Ergun, V. Angelopoulos, J. Bonnell, and K. H. Glassmeier. Solar wind influence on Pc4 and Pc5 ULF wave activity in the inner magnetosphere. *J. Geophys. Res.*, 115(A12), 2010.
- [58] W. Liu, T. E. Sarris, X. Li, Q.-G. Zong, R. Ergun, V. Angelopoulos, and K. H. Glassmeier. Spatial structure and temporal evolution of a dayside poloidal ULF wave event. *Geophys. Res. Lett.*, 38(19), 2011.
- [59] R. L. Lysak. Magnetosphere-ionosphere coupling by Alfvén waves at midlatitudes. *J. Geophys. Res.*, 109, 2004.
- [60] R. L. Lysak and D. hun Lee. Response of the dipole magnetosphere to pressure pulses. *Geophys. Res. Lett.*, 19(9):937–940, 1992.

- [61] R. L. Lysak and Y. Song. A three-dimensional model of the propagation of Alfvén waves through the auroral ionosphere: first results. *Adv. Space Res.*, 28:813–822, 2001.
- [62] R. L. Lysak, C. L. Waters, and M. D. Sciffer. Modeling of the ionospheric Alfvén resonator in dipolar geometry. *J. Geophys. Res. Space Physics*, 118, 2013.
- [63] P. N. Mager and D. Y. Klimushkin. Giant pulsations as modes of a transverse Alfvénic resonator on the plasmapause. *Earth, Planets and Space*, 65(5):397–409, 2013.
- [64] I. R. Mann, E. A. Lee, S. G. Claudepierre, J. F. Fennell, A. Degeling, I. J. Rae, D. N. Baker, G. D. Reeves, H. E. Spence, L. G. Ozeke, R. Rankin, D. K. Milling, A. Kale, R. H. W. Friedel, and F. Honary. Discovery of the action of a geophysical synchrotron in the Earth’s Van Allen radiation belts. *Nature Communications*, 4, 2013.
- [65] I. R. Mann and A. N. Wright. Finite lifetimes of ideal poloidal Alfvén waves. *J. Geophys. Res.*, 100:23677–23686, 1995.
- [66] I. R. Mann, A. N. Wright, and A. W. Hood. Multiple-timescales analysis of ideal poloidal Alfvén waves. *J. Geophys. Res.*, 102(A2):2381–2390, 1997.
- [67] T. Maynard, N. Smith, S. Gonzalez, et al. Solar storm risk to the North American electric grid. 2013.
- [68] K. McGuire, R. Goldston, M. Bell, M. Bitter, K. Bol, K. Brau, D. Buchenauer, T. Crowley, S. Davis, F. Dylla, H. Eubank, H. Fishman, R. Fonck, B. Grek, R. Grimm, R. Hawryluk, H. Hsuan, R. Hulse, R. Izzo, R. Kaita, S. Kaye, H. Kugel, D. Johnson, J. Manickam, D. Manos, D. Mansfield, E. Mazzucato, R. McCann, D. McCune, D. Monticello, R. Motley, D. Mueller, K. Oasa, M. Okabayashi, K. Owens, W. Park, M. Reusch, N. Sauthoff, G. Schmidt, S. Sesnic, J. Strachan, C. Surko, R. Slusher, H. Takahashi, F. Tenney, P. Thomas, H. Towner, J. Valley, and R. White. Study of high-beta magnetohydrodynamic modes and fast-ion losses in PDX. *Phys. Rev. Lett.*, 50(12):891–895, 1983.

- [69] R. L. McPherron. The role of substorms in the generation of magnetic storms. *Washington DC American Geophysical Union Geophysical Monograph Series*, 98:131–147, 1997.
- [70] R. L. McPherron, G. K. Parks, D. S. Colburn, and M. D. Montgomery. Satellite studies of magnetospheric substorms on august 15, 1968: 2. solar wind and outer magnetosphere. *J. Geophys. Res.*, 78(16):3054–3061, 1973.
- [71] T. Motoba, K. Takahashi, J. V. Rodriguez, and C. T. Russell. Giant pulsations on the afternoonside: Geostationary satellite and ground observations. *J. Geophys. Res. Space Physics*, 120:8350–8367, 2015.
- [72] NASA. Coordinated data analysis (workshop) web.
- [73] NASA. Near miss: The solar superstorm of july 2012.
- [74] M. Nicolet. The collision frequency of electrons in the ionosphere. *Journal of Atmospheric and Terrestrial Physics*, 3(4):200–211, 1953.
- [75] L. G. Ozeke and I. R. Mann. Energization of radiation belt electrons by ring current ion driven ULF waves. *J. Geophys. Res.*, 113(A2), 2008.
- [76] W. D. Pesnell. Predictions of solar cycle 24: How are we doing? *Space Weather*, 14(1):10–21, 2016.
- [77] E. M. Poulter, W. Allan, E. Nielsen, and K.-H. Glassmeier. Stare radar observations of a PG pulsation. *J. Geophys. Res.*, 88(A7):5668, 1983.
- [78] J. A. Proehl, W. Lotko, I. Kouznetsov, and S. D. Geimer. Ultralow-frequency magnetohydrodynamics in boundary-constrained geomagnetic flux coordinates. *J. Geophys. Res.*, 107(A9):1225, 2002.
- [79] H. R. Radoski. A note on oscillating field lines. *J. Geophys. Res.*, 72(1), 1967.
- [80] H. R. Radoski. A theory of latitude dependent geomagnetic micropulsations: The asymptotic fields. *J. Geophys. Res.*, 79, 1974.

- [81] R. Rankin, J. C. Samson, and V. T. Tikhonchuk. Parallel electric fields in dispersive shear alfvén waves in the dipolar magnetosphere. *Geophys. Res. Lett.*, 26(24):3601–3604, 1999.
- [82] B. Rolf. Giant micropulsations at abisko. *J. Geophys. Res.*, 36(1):9, 1931.
- [83] G. Rostoker, H.-L. Lam, and J. V. Olson. PC 4 giant pulsations in the morning sector. *J. Geophys. Res.*, 84(A9):5153, 1979.
- [84] J. C. Samson, L. L. Cogger, and Q. Pao. Observations of field line resonances, auroral arcs, and auroral vortex structures. *J. Geophys. Res.*, 101(A8):17373–17383, 1996.
- [85] H. J. Singer, W. J. Hughes, and C. T. Russell. Standing hydromagnetic waves observed by ISEE 1 and 2: Radial extent and harmonic. *J. Geophys. Res.*, 87(A5):3519, 1982.
- [86] D. J. Southwood. Some features of field line resonances in the magnetosphere. *Planetary and Space Science*, 22(3):483–491, 1974.
- [87] D. J. Southwood. A general approach to low-frequency instability in the ring current plasma. *J. Geophys. Res.*, 81(19):3340–3348, 1976.
- [88] J. Stratton and N. J. Fox. Radiation belt storm probes (RBSP) mission overview. In *2012 IEEE Aerospace Conference*. Institute of Electrical & Electronics Engineers (IEEE), 2012.
- [89] E. Sucksdorff. Giant pulsations recorded at sodankyl during 19141938. *Terrestrial Magnetism and Atmospheric Electricity*, 44(2):157–170, 1939.
- [90] K. Takahashi, J. Bonnell, K.-H. Glassmeier, V. Angelopoulos, H. J. Singer, P. J. Chi, R. E. Denton, Y. Nishimura, D.-H. Lee, M. Nosé, and W. Liu. Multipoint observation of fast mode waves trapped in the dayside plasmasphere. *J. Geophys. Res.*, 115(A12), 2010.
- [91] K. Takahashi, K.-H. Glassmeier, V. Angelopoulos, J. Bonnell, Y. Nishimura, H. J. Singer, and C. T. Russell. Multisatellite observations of a giant pulsation event. *J. Geophys. Res.*, 116:A11223, 2011.

- [92] K. Takahashi, M. D. Hartinger, V. Angelopoulos, K.-H. Glassmeier, and H. J. Singer. Multispacecraft observations of fundamental poloidal waves without ground magnetic signatures. *J. Geophys. Res. Space Physics*, 118:4319–4334, 2013.
- [93] K. Takahashi, R. W. McEntire, A. T. Y. Lui, and T. A. Potemra. Ion flux oscillations associated with a radially polarized transverse Pc 5 magnetic pulsation. *J. Geophys. Res.*, 95(A4):3717, 1990.
- [94] K. Takahashi, N. Sato, J. Warnecke, H. Lühr, H. E. Spence, and Y. Tonegawa. On the standing wave mode of giant pulsations. *J. Geophys. Res. Space Physics*, 97(A7):10717–10732, 1992.
- [95] B. J. Thompson and R. L. Lysak. Electron acceleration by inertial alfvén waves. *J. Geophys. Res.*, 101(A3):5359–5369, 1996.
- [96] S. M. Thompson and M. G. Kivelson. New evidence for the origin of giant pulsations. *J. Geophys. Res.*, 106(A10):21237–21253, 2001.
- [97] V. T. Tikhonchuk and R. Rankin. Electron kinetic effects in standing shear alfvén waves in the dipolar magnetosphere. *Physics of Plasmas*, 7(6):2630, 2000.
- [98] B. T. Tsurutani, W. D. Gonzalez, G. S. Lakhina, and S. Alex. The extreme magnetic storm of 12 september 1859. *Journal of Geophysical Research: Space Physics*, 108(A7), 2003. 1268.
- [99] A. Y. Ukhorskiy. Impact of toroidal ULF waves on the outer radiation belt electrons. *J. Geophys. Res.*, 110(A10), 2005.
- [100] J. Veldkamp. A giant geomagnetic pulsation. *Journal of Atmospheric and Terrestrial Physics*, 17(4):320–324, 1960.
- [101] C. L. Waters, R. L. Lysak, and M. D. Sciffer. On the coupling of fast and shear Alfvén wave modes by the ionospheric Hall conductance. *Earth Planets Space*, 65:385–396, 2013.
- [102] C. L. Waters and M. D. Sciffer. Field line resonant frequencies and ionospheric conductance: Results from a 2-d MHD model. *J. Geophys. Res.*, 113(A5), 2008.

- [103] D. M. Wright and T. K. Yeoman. High-latitude HF doppler observations of ULF waves: 2. waves with small spatial scale sizes. *Ann. Geophys.*, 17(7):868–876, 1999.
- [104] J. R. Wygant, A. Keiling, C. A. Cattell, R. L. Lysak, M. Temerin, F. S. Mozer, C. A. Kletzing, J. D. Scudder, V. Streitsov, W. Lotko, and C. T. Russell. Evidence for kinetic alfvn waves and parallel electron energization at 46 re altitudes in the plasma sheet boundary layer. *Journal of Geophysical Research: Space Physics*, 107(A8):SMP 24–1–SMP 24–15, 2002.
- [105] B. Yang, Q.-G. Zong, Y. F. Wang, S. Y. Fu, P. Song, H. S. Fu, A. Korth, T. Tian, and H. Reme. Cluster observations of simultaneous resonant interactions of ULF waves with energetic electrons and thermal ion species in the inner magnetosphere. *J. Geophys. Res.*, 115(A2), 2010.
- [106] K. Yee. Numerical solution of initial boundary value problems involving maxwell’s equations in isotropic media. *IEEE Trans. Antennas Propagat.*, 14(3), 1966.
- [107] T. K. Yeoman and D. M. Wright. ULF waves with drift resonance and drift-bounce resonance energy sources as observed in artificially-induced HF radar backscatter. *Ann. Geophys.*, 19(2):159–170, 2001.
- [108] Q.-G. Zong, X.-Z. Zhou, X. Li, P. Song, S. Y. Fu, D. N. Baker, Z. Y. Pu, T. A. Fritz, P. Daly, A. Balogh, and H. Réme. Ultralow frequency modulation of energetic particles in the dayside magnetosphere. *Geophys. Res. Lett.*, 34(12), 2007.
- [109] Q.-G. Zong, X.-Z. Zhou, Y. F. Wang, X. Li, P. Song, D. N. Baker, T. A. Fritz, P. W. Daly, M. Dunlop, and A. Pedersen. Energetic electron response to ULF waves induced by interplanetary shocks in the outer radiation belt. *J. Geophys. Res.*, 114(A10), 2009.